

Validation of the SensorVision Thermal Emission Model

Ninh Duong and Michael Wegener

DSTO-RR-0212

DISTRIBUTION STATEMENT A
Approved for Public Release
Distribution Unlimited

Validation of the SensorVision Thermal Emission Model

Ninh Duong and Michael Wegener

Weapons Systems Division
Aeronautical and Maritime Research Laboratory

DSTO-RR-0212

ABSTRACT

The Systems Simulation Centre of the DSTO is currently considering the implementation of a commercial-off-the-shelf software package called SensorVision to fulfil the scene generation function of an infrared hardware-in-the-loop (HIL) system. Before the software can be used for the intended application, there is a need to verify and validate the SensorVision models to ensure that the generated scenes are sufficiently realistic for HIL simulation purposes. This report discloses the results and conclusions of a validation effort focused on the SensorVision thermal emission model, which includes both the surface temperature prediction of objects and the thermal radiance calculations. It is shown that the thermal emission model employed by SensorVision has errors that can affect the level of realism associated with the generated infrared images. Unrealistic scenes can cause spurious HIL simulation results, since these infrared images are used as the primary stimuli for the system being tested.

A procedure for providing confidence in HIL simulation results is recommended, involving general guidelines for simulation construction and post-processing operations to provide users with image error indications.

RELEASE LIMITATION

Approved for public release

20010711 129

DEPARTMENT OF DEFENCE
DEFENCE SCIENCE & TECHNOLOGY ORGANISATION

DSTO

AQ F01-10-1751

Published by

*DSTO Aeronautical and Maritime Research Laboratory
PO Box 4331
Melbourne Victoria 3001 Australia*

Telephone: (03) 9626 7000

Fax: (03) 9626 7999

© Commonwealth of Australia 2001

AR-011-866

April 2001

APPROVED FOR PUBLIC RELEASE

Validation of the SensorVision Thermal Emission Model

Executive Summary

The validity of models used in the SSC's (Systems Simulation Centre) HIL (hardware-in-the-loop) facility at the DSTO has become an issue of recent concern. The results of a HIL simulation has only limited usefulness if there is low confidence in the ability of the HIL scene generators to produce realistic virtual environments. Both the target signature and background clutter, as well as any other significant signature effects, need to be faithfully reproduced by computational models. Confidence in HIL simulation results therefore, in part, requires confidence in the scene generator models.

In this report, the validation effort conducted on a COTS (commercial-off-the-shelf) software package called SensorVision is described. The SSC intends to employ SensorVision for the purpose of real-time image generation for HIL simulations involving imaging IR seekers. The physics-based model used by SensorVision to calculate the emitted radiance from solid objects due to thermal emission processes is scrutinised, and the temperature prediction model is validated against experimental data. The two main outcomes of this work are: a figure-of-merit parameter was developed to indicate the accuracy of the thermal emission model for any given simulation; and it was shown that the current version of the temperature prediction model is not appropriate for Australian climates and conditions.

Authors

Ninh Duong

Weapons Systems Division

Ninh Duong received a B.E. (Hons.) degree from the University of Adelaide in 1994. In 1998, he was awarded a Ph.D. degree from the University of Adelaide in the field of microwave and millimetre wave technology. In this research, theory was developed relating to the operation of millimetre wave power combining structures employing coupled oscillators. Ninh joined DSTO in 1998 and has been working on research pertaining to Hardware-In-The-Loop testing of infrared imaging and radar guided seekers. His research interests include power combining techniques, computational electromagnetics, microwave and millimetre wave technology, passive (IR and RF) imaging, target modelling, and real time scene generation. Ninh is an associate member of the IEEE.

Michael Wegener

Surveillance Systems Division

Michael Wegener received the degrees of Dipl.-Inform. (equiv. MSc. C.S.) and Dr.-Ing. (PhD EE) from the University of Hamburg, Germany, and the Federal Armed Forces University, Hamburg, in 1980 and 1984, respectively. In 1996, he received a Graduate Diploma in Management (Technology Management) from the Alfred Deakin University, Geelong. In his PhD Thesis, he modelled the colour and texture information processes in the human visual system from the pupil up to and including Area 19 of the visual cortex, and assessed the performance of the model for the pre-processing of aerial photography. Michael joined DSTO in 1988 and has since worked mainly in the areas of Image Processing and Electro optical Systems Analysis. His research interests include target, background clutter, and environment characterisation for passive electro optical systems performance analyses, and for real time Infrared Computer Image Generation for Hardware in the Loop Testing. Before joining DSTO he spent three years at The Flinders University of South Australia developing the hard- and software for a NOAA HRPT Satellite Receiver, and lecturing on topics in the areas of Data Analysis and Remote Sensing.

Related Publications by Authors

N. Duong, and M. Wegener, *SensorVision Radiometric Equations version 2.2*, DSTO report, DSTO-TN-0193, Feb. 1999.

N. Duong, and M. Wegener, "Assessment of the Radiometric Accuracy of SensorVision - First Results", *Proc. 4th Int. SimTecT Conf.*, pp. 295-300, Melbourne Aust., 29 Mar. - 1Apr. 1999.

N. Duong, and M. Wegener, "SensorVision Validation: Diurnal Temperature Variations in Northern Australia", *Proc. SPIE - Technologies for Synthetic Environments: Hardware-in-the-Loop Testing V*, Vol. 4027, pp. 329-340, Orlando Florida USA, 24-28 Apr. 2000.

Table of Contents

| | |
|---|-------------|
| Table of Contents | ix |
| List of Figures | xi |
| List of Tables | xiii |
| Abbreviations | xv |
| Notation | xvii |
| 1. Introduction | 1 |
| 1.1 Infrared Scene Generation and SensorVision | 1 |
| 1.2 Verification and Validation | 3 |
| 1.3 Proposed Validation Procedures for HIL Simulations | 4 |
| 1.4 Report Outline | 5 |
| 2. Validation of the Thermal Emission Model | 7 |
| 2.1 The SensorVision Thermal Emission Model | 7 |
| 2.2 Figure of Merit using the Second Moment | 11 |
| 2.3 Effect of Variability of Material Emissivity | 12 |
| 2.4 Effect of Variability of Atmospheric Transmission Coefficient | 19 |
| 2.5 Effect of Variability of Planck's Blackbody Curve | 25 |
| 2.6 Chapter Summary | 27 |
| 3. Validation of the Temperature Prediction Model | 29 |
| 3.1 The SensorVision Temperature Prediction Model | 29 |
| 3.2 Processing of Experimental Data | 32 |
| 3.3 Validation of Temperature Prediction Model | 37 |
| 3.4 Chapter Summary | 45 |
| 4. Conclusions and Further Work | 47 |
| 5. References | 49 |
| Appendix A: Using Error Indicators | 51 |
| A.1 Error Indicators for Material Emissivities | 51 |
| A.2 Error Indicators for the Atmospheric Transmission Coefficient | 54 |
| A.3 Error Indicators for Planck's Blackbody Spectral Radiance | 56 |
| A.4 Combining Error Indicator Values | 57 |
| A.5 Equations for Calculating the Second Moment | 57 |

DSTO-RR-0212

List of Figures

| | |
|--|----|
| Figure 1-1: IR HIL system. | 1 |
| Figure 1-2: COTS based IRSG system. | 3 |
| Figure 2-1: Bar graphs showing the relative error caused by the SensorVision thermal emission model as a function of material for (a) the MWIR band and (b) the LWIR band. The temperature is assumed to be 300 K and the atmospheric transmission coefficient is assigned a value of unity. | 13 |
| Figure 2-2: Bar graphs showing the error in effective temperature caused by the SensorVision thermal emission model as a function of material for (a) the MWIR band and (b) the LWIR band. The temperature is assumed to be 300 K and the atmospheric transmission coefficient is assigned a value of unity. | 15 |
| Figure 2-3: Bar graphs of second moments of material emissivities for (a) the MWIR band, and (b) the LWIR band. | 16 |
| Figure 2-4: Plot of atmospheric transmission coefficient as a function of wavelength for a selection of LOS paths: (a) a horizontal 1 km path; (b) a horizontal 10 km path; (c) a vertical 1 km path; and (d) a vertical 50 km path. | 22 |
| Figure 2-5: Plot of Planck's blackbody curves as a function of temperature. | 25 |
| Figure 2-6: Mean relative error between SensorVision thermal emission model and exact model as a function of temperature. Atmospheric transmission coefficient is assumed to be unity and all 110 materials are included in the computation of the mean relative error. | 26 |
| Figure 2-7: Plot of error indicator value of Planck's blackbody curve in waveband of interest as a function of temperature. | 26 |
| Figure 3-1: Plots of the (a) raw, (b) filtered, and (c) the statistics of the data sample space for measured air and concrete daily temperature profiles for the month of April (1991, 1992, and 1993). The data statistics are plotted as error bars with a mean and an error of one standard deviation. | 34 |
| Figure 3-2: Examples of the temperature profile comparisons used to identify outliers: (a) temperature profiles for 28 April 1992, and (b) temperature profiles for the 5 February 1992, showing an outlier in the sensor #2 concrete temperature profile. | 35 |
| Figure 3-3: Diagram showing the days of the year for which the MAT predicts identical daily temperature profiles. | 38 |

| | |
|--|----|
| Figure 3-4: Comparisons of the MAT generated results with mean 9 a.m. and 3 p.m. air temperatures obtained from the (Australian) Bureau of Meteorology. | 39 |
| Figure 3-5: Comparison between the MAT generated and measured diurnal air temperature profiles for the months from February to November. | 40 |
| Figure 3-6: Comparison between the MAT generated and measured diurnal concrete temperature profiles for the months from February to November. | 41 |
| Figure 3-7: Graphs illustrating the effect of varying heat transfer parameters on the MAT predicted concrete diurnal temperature profiles for the month of April. ... | 42 |
| Figure 3-8: Comparison between the MAT results with modified concrete heat transfer parameters and measured diurnal concrete temperature profiles. | 44 |

List of Tables

| | |
|---|----|
| Table 2-1: List of materials tested in validation and associated material codes. | 14 |
| Table 2-2: Emissivity error indicator values for materials. | 18 |
| Table 2-3: List of LOS paths tested in validation of SensorVision thermal emission model. | 20 |
| Table 2-4: Error indicator values for LOS paths tested. | 21 |
| Table 2-5: Summary of errors generated by SensorVision thermal emission model including both material emissivity and atmospheric transmission coefficient data. Errors are represented in terms of percentage error (ΔL) relative to the exact radiance, and the difference (ΔT) between SensorVision and exact effective temperatures. | 24 |
| Table 3-1: List of heat transfer parameters. | 30 |
| Table 3-2: List of the MAT input file parameters. | 31 |
| Table 3-3: List of days during 1991, 1992, and 1993 in which some temperature measurements were recorded. | 33 |
| Table 3-4: Summary of sample space sizes for each month listing the number of raw data sets, the number of data sets that were incomplete or contained outliers, and the final total sample space size. | 36 |
| Table 3-5: List of original and modified heat transfer parameters. | 43 |
| Table A-1: Emissivity mean and second moment values for different composite materials. | 51 |
| Table A-2: Emissivity mean and second moment values for different construction materials. | 52 |
| Table A-3: Emissivity mean and second moment values for different types of paints. | 52 |
| Table A-4: Emissivity mean and second moment values for different types of soils. | 53 |

Table A-5: Emissivity mean and second moment values for different types of
vegetation. 54

Table A-6: Second moment and mean values for transmission coefficients of some LOS
paths. 55

Table A-7: Second moment values for the normalised Planck’s blackbody spectral
radiance. 56

Abbreviations

| | Definition |
|--------|--|
| 2-D | two dimensional |
| 3-D | three dimensional |
| COTS | commercial-off-the-shelf |
| DC | direct current |
| DSTO | Defence Science and Technology Organisation |
| EI | error indicator |
| GMT | Greenwich Mean Time |
| IR | infrared |
| IRSG | infrared scene generator |
| IRSP | infrared scene projector |
| LWIR | long wave infrared |
| LOS | line of sight |
| LST | local standard time |
| MAT | MOSART Atmospheric Tool |
| MOSART | Moderate Spectral Atmospheric Radiance and Transmittance |
| MWIR | mid-wave infrared |
| RMS | root mean square |
| SSC | Systems Simulation Centre |
| SUT | system under test |
| TERTEM | Terrain Temperatures |
| TMM | Texture Material Mapper |
| U.S. | United States |
| V&V | verification and validation |
| WSD | Weapons Systems Division |

Notation

| Symbol | Definition | Units |
|------------------------|---|-------------------------------|
| ε_λ | material spectral emissivity | |
| $\bar{\varepsilon}$ | mean value of emissivity data | |
| λ | wavelength | μm |
| π | circle circumference to diameter ratio (3.14159) | |
| ρ_λ | material spectral reflectivity | |
| τ_λ | spectral atmospheric transmission coefficient | |
| $\bar{\tau}$ | mean value of transmission coefficient data | |
| Φ_λ | spectral response of a sensor | |
| c_1 | radiation constant (3.7418×10^8) | $\text{Wm}^{-2}\mu\text{m}^4$ |
| c_2 | radiation constant (1.438769×10^4) | μmK |
| EI_ε | error indicator for material emissivity | |
| $EI_{\varepsilon\tau}$ | error indicator for emissivity and transmission coefficient product | |
| EI_τ | error indicator for atmospheric transmission coefficient | |
| EI_{bb} | error indicator for Planck's blackbody curve | |
| EI_{total} | error indicator for SensorVision thermal emission model | |
| e | second moment | |
| e_ε | second moment for emissivity data | |
| $e_{\varepsilon\tau}$ | second moment for emissivity and transmission coefficient product | |
| e_τ | second moment for transmission coefficient data | |

| Symbol | Definition | Units |
|-------------------------|---|--|
| <i>error</i> | relative error between exact and SensorVision calculated radiance | |
| L^{exact} | exact radiance | $\text{Wm}^{-2}\text{sr}^{-1}$ |
| L^{SV} | radiance calculated by SensorVision model | $\text{Wm}^{-2}\text{sr}^{-1}$ |
| L_{λ}^{bb} | Planck's blackbody spectral radiance | $\text{Wm}^{-2}\text{sr}^{-1}\mu\text{m}^{-1}$ |
| $L_{\lambda}^{emitted}$ | emitted spectral radiance | $\text{Wm}^{-2}\text{sr}^{-1}\mu\text{m}^{-1}$ |
| L_{λ}^{sensor} | spectral radiance detected by a sensor | $\text{Wm}^{-2}\text{sr}^{-1}\mu\text{m}^{-1}$ |
| T | temperature | K |
| T_{eff} | effective temperature | K |

1. Introduction

1.1 Infrared Scene Generation and SensorVision

The SSC (Systems Simulation Centre) is currently in the process of upgrading the HIL (hardware-in-the-loop) facility at the DSTO (Defence Science and Technology Organisation) to enable the test and evaluation of imaging IR (infrared) seekers. The upgrade consists of two main components:

- the acquisition and integration of an IRSP (infrared scene projector) into the existing system; and
- the development of an IRSG (infrared scene generator) capable of real-time IR image generation.

The proposed HIL system is shown schematically in Figure 1-1. The subsystem of main interest in this report is the IRSG. The functions of the IRSG are two-fold: first, it is responsible for creating and maintaining the 3-D (three-dimensional) virtual

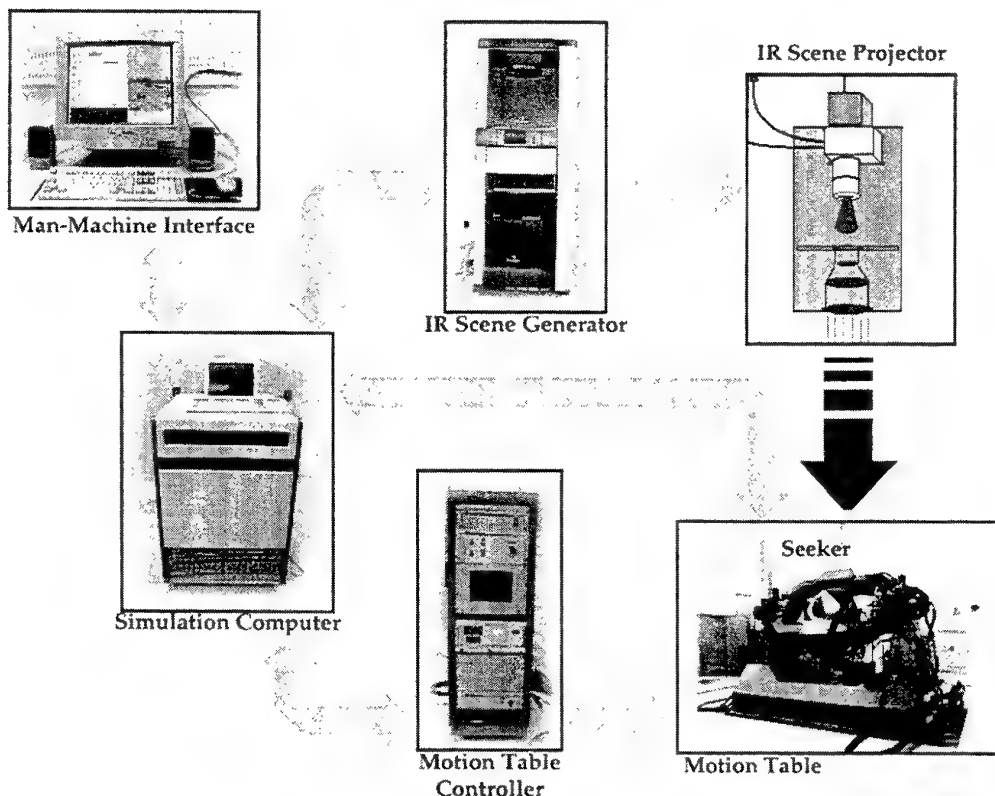


Figure 1-1: IR HIL system.

environment within which the seeker is to be immersed; and second, it renders that environment into the 2-D (two-dimensional) images used to stimulate the seeker via the IRSP.

The requirements of the combined IRSG and IRSP modules are demanding in that the IR scenes used to stimulate the seeker must be realistic, and the image framerates can be extremely high (in excess of 100 Hz for some air-to-air seekers). The former criterion is somewhat ambiguous because it is dependent on the SUT (system under test). The scenes only need to be realistic enough such that the SUT performs in a manner consistent with a real-life engagement. Given the diversity of current and future IR seekers that may be tested within the HIL facility, the policy adopted by the DSTO is to ensure that the scenes used to stimulate the seeker are as realistic as possible given other critical constraints (such as cost, effort, and the requirement for real-time performance).

The quality of scenes and the rate of image generation is initially controlled by the IRSG. The IRSP may then degrade the scenes and affect the framerate, depending on the capabilities of the unit. In addition, various IRSP induced artifacts may occur. This report will only consider the IRSG.

The IRSG system that is currently being evaluated in the SSC is a COTS (commercial-off-the-shelf) based system. The decision to pursue a COTS solution was primarily motivated by cost considerations. The purchase and maintenance of commercial products is generally more cost effective than the in-house development of custom products. The IRSG system, which is shown in Figure 1-2, uses an SGI™ Onyx2™ computer platform with an InfiniteReality2™ graphics engine. A real-time visual simulation tool called Vega™ is used to control the simulations and perform the rendering operations. Vega is built upon the graphics languages OpenGL™ and Performer™. SensorVision™ is a Vega add-on module, which enables Vega to perform IR simulations. SensorVision contains the physics-based models required to compute the radiometric IR images associated with the virtual environment. Both Vega and SensorVision are distributed by MultiGen-Paradigm™ Incorporated.

SensorVision is a real-time IR signature prediction package, which uses various approximations to enable real-time computations. The nature of these approximations are described in detail in reference [1]. This report focuses on the validation of the SensorVision thermal emission model, which includes both the surface temperature prediction of objects in the scene and the thermal emission radiance computation.

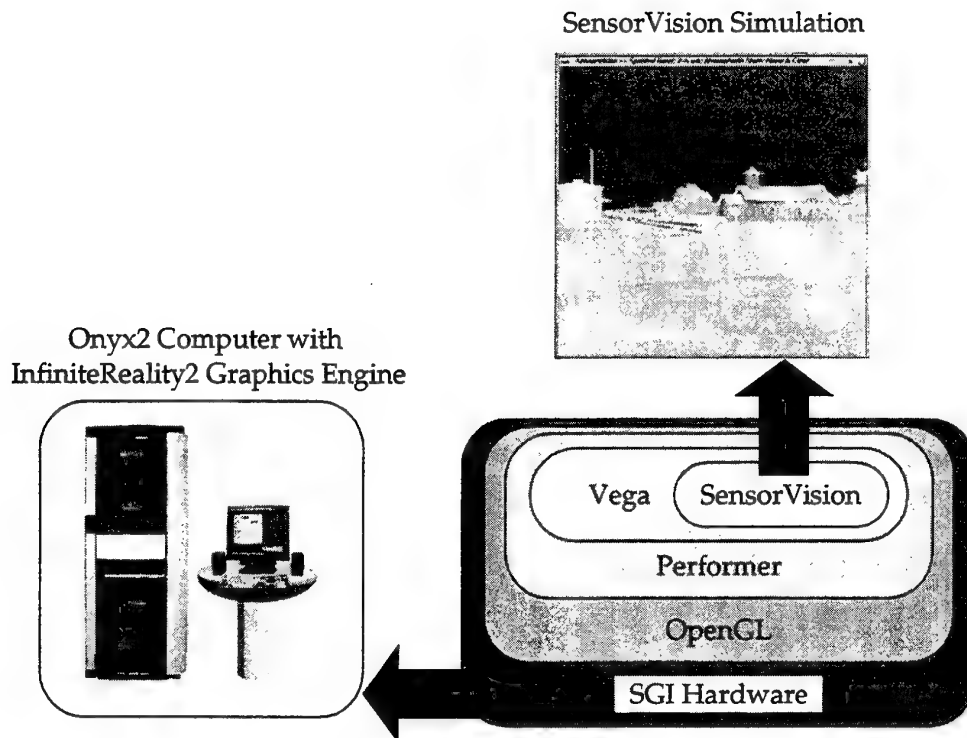


Figure 1-2: COTS based IRSG system.

1.2 Verification and Validation

The concept of verification and validation (V&V) is frequently encountered in a range of different engineering disciplines, but the distinct differences between the two terms are often not clearly understood.

- Verification determines the accuracy and consistency of software algorithms compared to the underlying mathematical models [2]. A verified software program should be algorithmically correct and any numerical methods used should lead to solutions having the accuracy required by the application. Verification is often associated with software debugging procedures.
- Validation is a more fundamental concept in that it considers the relationship between the underlying mathematical model and the real world system upon which it is based [2]. In other words, validation is concerned with how well models represent real physical processes.

Ideally, it should not be necessary to verify commercial software since it is normal to assume that quality assurance practices and software testing procedures in a commercial

establishment are sufficiently comprehensive to ensure reasonably bug-free programs. Consequently, the verification of SensorVision is not considered to any depth within this report and the validation of SensorVision is the main focus.

With validation, there are two main model attributes that are of concern: accuracy, and realism. Accuracy refers to the ability of a model to correctly characterise some physical process, while realism additionally requires all significant and relevant physics to be modelled. For example, a model may characterise thermal emission processes accurately, but if reflection phenomena are ignored, the model may be not be realistic.

In general, there are two strategies¹ that can be adopted in a validation effort:

- Mathematical validation involves the comparison of data obtained from the model with data obtained from other (non-real-time) models that are considered accurate. Mathematical validation is primarily concerned with the accuracy of the models.
- Experimental validation involves the comparison of model generated results against experimentally measured data. Experimental validation may also consider the realism of the model as well as the accuracy aspects.

The SensorVision validation will be conducted from both mathematical and experimental perspectives. However, because mathematical validation is the more economical and less labour intensive option, this strategy will mainly be applied.

1.3 Proposed Validation Procedures for HIL Simulations

The purpose and aim of a validation program are often difficult to articulate. In most cases, models are not perfect and there are difficult questions to answer in relation to how results from a validation program should be interpreted. In particular, with respect to HIL simulations and the IRSG function, some pertinent questions include:

- How realistic does the SensorVision models and resultant generated images have to be?
- What are the effects of artifacts in the virtual environment on the response of the seeker?

These questions can only be answered by experts with intimate knowledge of the subsystems of the seeker being tested, given sufficient information. With this truth in mind, a two tier approach to the validation program is proposed.

First, the validation effort should be conducted with a view to develop general guidelines that could be employed during the simulation construction phase of a HIL procedure. For example, simple guidelines could be used to identify conditions that are

¹. Obviously, both validation strategies assume verified models. An unverified model may generate incorrect results due to errors in the algorithm code thus it cannot be properly validated.

likely to cause erroneous or unrealistic scenes. These conditions could then be avoided in the simulation.

Second, some post-simulation validation procedure should be developed to enable users of HIL simulations to form opinions as to the validity of a set of HIL results. Ideally, some measure of quality should be provided to indicate the sorts of errors associated with the simulation. Furthermore, it would be advantageous if the origins of the errors are also provided. The most promising idea is to formulate a procedure whereby frame grabs are obtained at various instances during a simulation. In post-simulation operations, those same frames are processed again using accurate non-real-time models. A certain amount of confidence needs to be placed in the ability of the non-real-time models to produce accurate and realistic images. An error frame showing radiometric error figures (between the SensorVision generated results and the non-real-time accurate model) could then be generated and presented to experts for evaluation.

The proposed two tier approach should be sufficient for realistic HIL simulations to be created and subsequently evaluated.

1.4 Report Outline

This report consists of two distinct sections. Chapter 2 discusses the validation effort associated with the SensorVision model used to compute the emitted radiance from an object due to thermal emission. The model is mathematically validated against an accurate non-real-time model, and a measure of quality figure is developed. This measure of quality can be used during the simulation construction phase to rapidly assess the likely level of errors associated with that particular simulation. In addition, general guidelines are developed to indicate simulation scenarios that should be avoided to minimise SensorVision generated errors.

The second main component of the report, which discusses the validation of the temperature prediction model used by SensorVision, is presented in Chapter 3. The temperature prediction model is validated against experimental data obtained from trials conducted in Northern Australia. Measured temperature diurnal profiles are compared against SensorVision generated results and conclusions are formulated based on these results.

The validation described in Chapter 2 and Chapter 3 provides an excellent indication of SensorVision's ability to model signature components due to thermal emission processes. The realism aspects of SensorVision are not really considered in this report since reflection and path scattering processes are not validated. Chapter 4 provides a summary of conclusions and recommendations for further work.

2. Validation of the Thermal Emission Model

2.1 The SensorVision Thermal Emission Model

Reference [1] describes in detail the thermal emission model employed by SensorVision. The model is an equation that computes the radiance received by a sensor due to thermal emission processes from a material with a surface temperature, T . The models used to predict the surface temperature T is discussed in Chapter 3.

The SensorVision thermal emission model is based on the following physics. Fundamentally, the emitted radiance¹ from any solid surface is described in terms of the thermal emission from a blackbody. The blackbody is an idealised material, with properties that make it a perfect absorber and a perfect radiator. All energy incident on a blackbody is completely absorbed and consequently radiated in order to maintain thermal equilibrium. The spectral radiance (L_{λ}^{bb}) emitted from a blackbody of temperature (T) is modelled by the well known Planck's blackbody equation, and is given by

$$L_{\lambda}^{bb} = \frac{c_1}{\pi \lambda^5 \left(e^{\frac{c_2}{\lambda T}} - 1 \right)} \quad (\text{Wm}^{-2} \text{sr}^{-1} \mu\text{m}^{-1}). \quad (2-1)$$

The parameters c_1 and c_2 are radiation constants, and are given by

$$c_1 = 3.7418 \times 10^8 \quad (\text{Wm}^{-2} \mu\text{m}^4), \text{ and} \quad (2-2)$$

$$c_2 = 1.438769 \times 10^4 \quad (\mu\text{mK}), \text{ respectively.} \quad (2-3)$$

The subscript " λ " is used to indicate the wavelength dependence of the blackbody spectral radiance. The integration of (2-1) over waveband of interest yields the radiance emitted from a blackbody within that waveband. For a real material, a property referred to as the spectral emissivity (ϵ_{λ}) represents the material's efficiency of emission relative to a blackbody radiator. Assuming the material is Lambertian², the spectral radiance emitted by the material is given by

¹ Radiance is the fundamental unit of infrared physics. Radiance (or sterance) is defined as the power per unit projected area per unit solid angle.

² A Lambertian material is one in which the radiance emitted by the material is independent of the observation angle. In other words, a Lambertian material is an isotropic radiator with respect to radiance (not intensity). Lambertian materials are also often described as diffuse.

$$L_{\lambda}^{emitted} = \epsilon_{\lambda} L_{\lambda}^{bb}. \quad (2-4)$$

If the material is opaque so that transmission processes are neglected then the relationship between spectral emissivity and spectral reflectivity³ (ρ_{λ}) is given by

$$\epsilon_{\lambda} = 1 - \rho_{\lambda}. \quad (2-5)$$

Equation (2-5) is simply a statement of the conservation of energy. Taking into account the spectral response of the sensor⁴ (ϕ_{λ}) and the atmospheric transmission coefficient (τ_{λ}) along the LOS (line of sight) path between the material and the sensor, the spectral radiance detected by the sensor is given by

$$L_{\lambda}^{sensor} = \phi_{\lambda} \tau_{\lambda} \epsilon_{\lambda} L_{\lambda}^{bb}. \quad (2-6)$$

The radiance detected over the waveband λ_1 to λ_2 is given by

$$L^{exact} = \int_{\lambda_1}^{\lambda_2} \phi_{\lambda} \tau_{\lambda} \epsilon_{\lambda} L_{\lambda}^{bb} d\lambda \quad (\text{Wm}^{-2}\text{sr}^{-1}). \quad (2-7)$$

Equation (2-7) is the generally accepted physically accurate equation for calculating the radiance incident on a sensor due to thermal emission processes, and will be referred to as the "exact" model. The radiating material is assumed to be Lambertian, opaque, and solid. Note that thermal emissions due to the atmosphere along the LOS path from the material to the sensor are not modelled by (2-7). SensorVision separates the thermal emissions due to the atmospheric path from the emissions due to solid opaque materials [1].

The problem with employing (2-7) in a real-time signature prediction code is that the equation involves a spectral integration, which is computationally time consuming to evaluate. Consequently, SensorVision uses various approximations to increase the speed with which the thermal emission quantities can be calculated. The SensorVision thermal emission model is based on the equation

-
- ³. Spectral reflectivity is the property of a surface that specifies the amount of spectral irradiance (total spectral radiance incident on the surface area) reflected by the surface. It is defined as the ratio of the spectral exitance (total spectral radiance reflected by total surface area) to the spectral irradiance.
- ⁴. The parameter (ϕ_{λ}) is used by SensorVision to crudely model any attributes of the sensor that causes frequency selectivity in its response. The parameter may include the lumped effect of transmission through the sensor optics, detector responsivity, or any other frequency selective sensor property.

$$L^{SV} = \bar{\tau}\bar{\epsilon}\int_{\lambda_1}^{\lambda_2}\varphi_{\lambda}L_{\lambda}^{bb}d\lambda. \quad (2-8)$$

In comparison to (2-7), the spectral terms τ_{λ} and ϵ_{λ} have been moved outside of the spectral integration and replaced by their in-band averaged values $\bar{\tau}$ and $\bar{\epsilon}$. The bar notation is used to denote the averaging (mean) function. The integration term in (2-8) is essentially precomputed as a function of temperature, and stored in a multivariate database (or lookup table). Consequently, the SensorVision thermal emission model involves only fast multiplication calculations so that it can be executed in real-time. The direct comparison of (2-7) to (2-8) constitutes a mathematical validation. The determination of whether the use of lookup tables is accurate is a verification activity. Only the mathematical validation of the SensorVision thermal emission model will be considered in this report.

The manipulation from (2-7) to (2-8) is valid only if the spectral atmospheric transmission coefficient and the material's spectral emissivity are constant within the waveband of interest. Interestingly, the approximation is also valid if the argument of the spectral integration ($\varphi_{\lambda}L_{\lambda}^{bb}$) is constant within the waveband of interest. The proof for this statement is as follows:

Consider the following substitution

$$L_{\lambda} = \varphi_{\lambda}L_{\lambda}^{bb}. \quad (2-9)$$

With this substitution, (2-8) can be expressed in the form

$$L^{SV} = \bar{\tau}\bar{\epsilon}\int_{\lambda_1}^{\lambda_2}L_{\lambda}d\lambda, \quad (2-10)$$

where the superscript "SV" indicates that the equation refers to the SensorVision implemented form of the thermal emission equation. If L_{λ} has a constant value L within the waveband of interest, then

$$L^{SV} = \bar{\tau}\bar{\epsilon}L\int_{\lambda_1}^{\lambda_2}d\lambda \quad (2-10a)$$

$$\Rightarrow L^{SV} = \bar{\tau}\bar{\epsilon}L(\lambda_2 - \lambda_1). \quad (2-10b)$$

Now consider (2-7) expressed in the form

$$L^{exact} = \int_{\lambda_1}^{\lambda_2} \tau_{\lambda} \epsilon_{\lambda} L_{\lambda} d\lambda. \quad (2-11)$$

If L_{λ} is again constant within the waveband of interest, then

$$L^{exact} = L \int_{\lambda_1}^{\lambda_2} \tau_{\lambda} \epsilon_{\lambda} d\lambda \quad (2-11a)$$

$$\Rightarrow L^{exact} = L \int_{\lambda_1}^{\lambda_2} \tau_{\lambda} \epsilon_{\lambda} d\lambda \frac{(\lambda_2 - \lambda_1)}{(\lambda_2 - \lambda_1)} \quad (2-11b)$$

$$\Rightarrow L^{exact} = L \left[\frac{\int_{\lambda_1}^{\lambda_2} \tau_{\lambda} \epsilon_{\lambda} d\lambda}{(\lambda_2 - \lambda_1)} \right] (\lambda_2 - \lambda_1) \quad (2-11c)$$

$$\Rightarrow L^{exact} = L \bar{\tau} \bar{\epsilon} (\lambda_2 - \lambda_1) \quad (2-11d)$$

$$\Rightarrow L^{exact} = L \bar{\tau} \bar{\epsilon} (\lambda_2 - \lambda_1) \quad (2-11e)$$

$$\Rightarrow L^{exact} = L^{SV}. \quad (2-11f)$$

Consequently, it can be concluded that the SensorVision thermal emission equation (2-8) is exactly equivalent to the accurate equation (2-7) if the term $\phi_{\lambda} L_{\lambda}^{bb}$ is constant within the waveband of interest. Note that the step from (2-11d) to (2-11e) requires the variables τ_{λ} and ϵ_{λ} to be independent. Given that the emissivity is a material property and the transmission coefficient is an atmospheric property, the variables τ_{λ} and ϵ_{λ} are clearly independent.

To reiterate, the SensorVision equation is equivalent to the accurate thermal emission equation:

- if the spectral atmospheric transmission coefficient and the material's spectral emissivity are constant within the waveband of interest; or
- if the argument of the spectral integration $\phi_{\lambda} L_{\lambda}^{bb}$ is constant within the waveband of interest.

In this validation effort, it is assumed that the spectral response of the sensor is unity so that the argument of the spectral integration is simply the spectral blackbody radiance.

2.2 Figure of Merit using the Second Moment

Mathematical validation of the SensorVision thermal emission equation essentially involves the determination of the level of errors associated with the approximation described in Section 2.1. In this approximation, spectral terms are moved outside of the spectral integration and replaced by their in-band averaged values. From the discussion in Section 2.1, the level of errors associated with the SensorVision thermal emission model is clearly dependent on:

- the variability of the material's spectral emissivity in the waveband of interest;
- the variability of the spectral atmospheric transmission coefficient in the waveband of interest; and
- the variability of the spectral blackbody radiance in the waveband of interest (assuming the spectral response of the sensor is unity).

In Section 1.3, a two tier validation strategy for HIL simulations was proposed. In the first tier involving the use of guidelines for simulation construction, some figure of merit should ideally be defined to enable the rapid assessment of likely error levels given details of the simulation. Since the error levels are primarily dependent on the variability of several spectral parameters, the figure of merit should logically be based on the second moment or RMS (root mean square) error. The second moment is a value often used in mathematics to express the variability of a function or parameter. The second moment is defined by the equation

$$e = \sqrt{(\Delta x)^2}, \quad (2-12)$$

where Δx is the difference between the value x_λ and the mean value \bar{x} . For a continuous variable, the second moment can be calculated using

$$e = \sqrt{\frac{\int_{\lambda_1}^{\lambda_2} (x_\lambda - \bar{x})^2 d\lambda}{(\lambda_2 - \lambda_1)}}, \quad (2-13)$$

while the equation relevant for a discrete variable $x_\lambda(n)$ with N samples is

$$e = \sqrt{\frac{1}{N} \sum_{n=1}^N [x_\lambda(n) - \bar{x}]^2}. \quad (2-14)$$

During the SensorVision validation effort, the second moment will be used to develop general guidelines for simulation construction.

2.3 Effect of Variability of Material Emissivity

The first step in the validation effort was to determine the effect of variability in the material's spectral emissivity on the SensorVision thermal emission model. This task was accomplished by comparing radiance values computed using (2-7) and (2-8) for a range of materials. Two wavebands are of primary concern: the MWIR (mid-wave infrared) band; and the LWIR (long-wave infrared) band. The MWIR band nominally spans the waveband from 3 μm to 5 μm , and is the band usually exploited in air-to-air missiles. Hot exhaust plumes and hot engine parts tend to be very visible in the MWIR band. The LWIR band extends from about 8 μm to 12 μm , and is the band often used in the imaging of ground based scenes. Thermal emission processes dominate in the LWIR band, and it is the waveband in which thermal differences between objects with temperatures near ambient (≈ 300 K) can be most efficiently detected. In the following validation, the atmospheric transmission coefficient is assumed to be equal to one and a material temperature of 300 K is used. Consequently, the modified exact and SensorVision equations are

$$L^{exact} = \int_{\lambda_1}^{\lambda_2} \epsilon_{\lambda} L_{\lambda}^{bb} d\lambda, \text{ and} \quad (2-15)$$

$$L^{SV} = \bar{\epsilon} \int_{\lambda_1}^{\lambda_2} L_{\lambda}^{bb} d\lambda, \text{ respectively.} \quad (2-16)$$

The error between the SensorVision and exact models for a range of materials were computed, and are plotted in the bar graphs of Figure 2-1. The errors are represented relative to the exact radiance values according to

$$error = \frac{L^{SV} - L^{exact}}{L^{exact}}. \quad (2-17)$$

A total of 110 materials were tested including various composites, soils, vegetation, construction materials, and paints. These 110 materials represent the entire materials database packaged with SensorVision version 2.2. The emissivity (or reflectivity) data used in the computations were the default data for the materials included with the SensorVision package. These data are claimed to be representative of typical materials. The materials are labelled along the x-axis of the bar graphs in Figure 2-1 and are identified by their material codes. Table 2-1 contains the material descriptions with their codes.

Figure 2-1(a) shows the SensorVision errors associated with the MWIR band. As can be seen, the errors fluctuate significantly depending on the material. A relative error of 22.7 % is associated with the material oxidised aluminium. In comparison, the errors shown in Figure 2-1(b) for the LWIR band are negligible. These errors are only a fraction of a percent for all materials tested. Despite these results, it is not prudent to immediately conclude that SensorVision is ill-suited to the MWIR band and well-suited to the LWIR band. In fact, these results have a temperature dependence and the low errors associated with the LWIR band is mainly due to the chosen temperature of 300 K. The temperature dependence will be explained in greater detail in Section 2.5. For now, it suffices to state that no definite conclusions can be drawn from the results plotted in Figure 2-1, besides

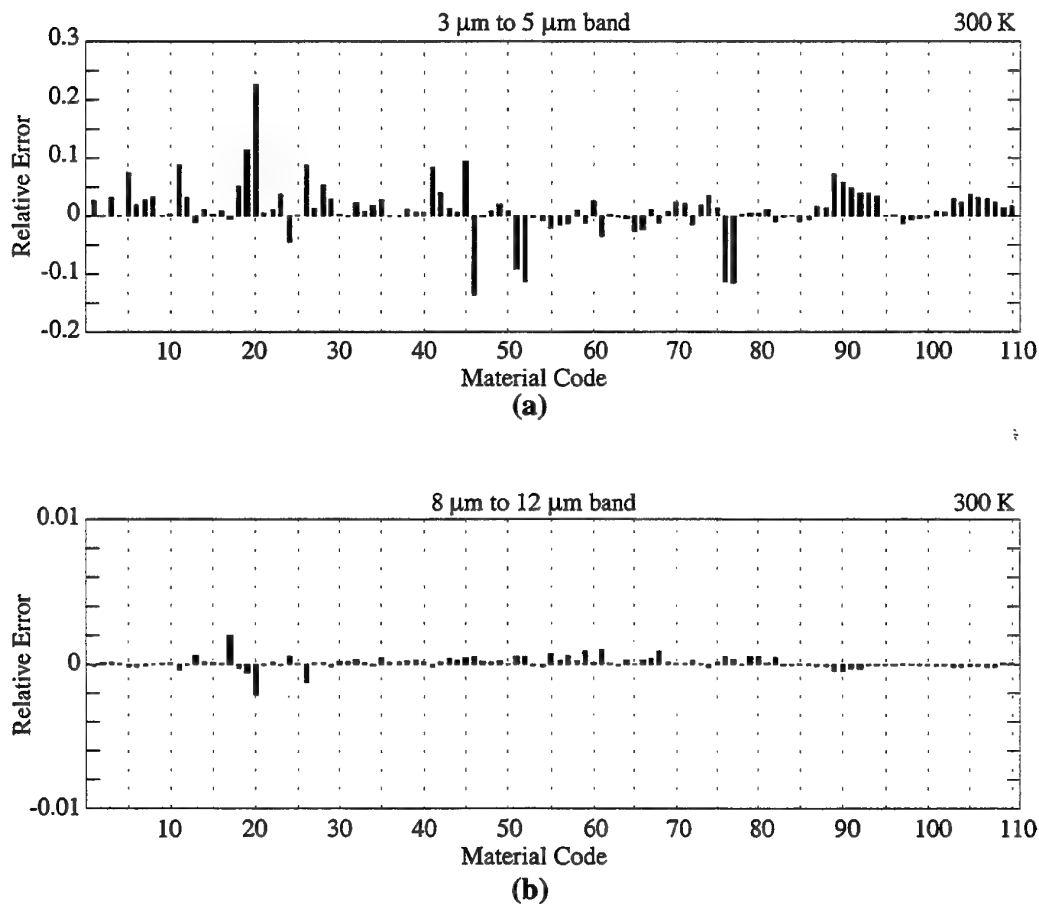


Figure 2-1: Bar graphs showing the relative error caused by the SensorVision thermal emission model as a function of material for (a) the MWIR band and (b) the LWIR band. The temperature is assumed to be 300 K and the atmospheric transmission coefficient is assigned a value of unity.

| Code | Material | Code | Material | Code | Material |
|------|---------------------|------|---------------------|------|---------------------------|
| | COMPOSITES | | SOILS | | VEGETATION |
| 1 | beige_fabric | 46 | beach_sand | 83 | broadleaf |
| 2 | black_rubber | 47 | black_sand | 84 | broadleaf (shaded) |
| 3 | brown_plastic | 48 | clay_soil | 85 | broadleaf-pine |
| 4 | cream_fiberglass | 49 | compact_soil | 86 | broadleaf-pine (shaded) |
| 5 | gold_nylon | 50 | desert_sand | 87 | broadleaf-scrub |
| 6 | green_canvas | 51 | dry_lakebed | 88 | broadleaf-scrub (shaded) |
| 7 | grey_fabric | 52 | dry_seabed | 89 | dry_grass |
| 8 | olive_plastic | 53 | fresh_snow | 90 | dry_grass (shaded) |
| 9 | orange_epoxy | 54 | ice | 91 | grass-scrub |
| 10 | red_nylon | 55 | lake_sand | 92 | grass-scrub (shaded) |
| 11 | tan_felt | 56 | limestone-silt | 93 | grass-soil |
| 12 | white_fabric | 57 | limestone-silt-sand | 94 | grass-soil (shaded) |
| 13 | yellow_silicon | 58 | limestone-silt-soil | 95 | lawn_grass |
| 14 | asphalt_shingles | 59 | limestone_rock | 96 | lawn_grass (shaded) |
| | CONSTRUCTION | 60 | loam_soil | 97 | pine |
| 15 | black_asphalt | 61 | loamy_sand | 98 | pine (shaded) |
| 16 | block_concrete | 62 | lump_coal | 99 | pine-broadleaf |
| 17 | clear_glass | 63 | old_snow | 100 | pine-broadleaf (shaded) |
| 18 | dark_titanium | 64 | road_gravel | 101 | pine-scrub |
| 19 | metal_roof | 65 | salt-silt | 102 | pine-scrub (shaded) |
| 20 | oxydized_aluminum | 66 | sand-soil | 103 | scrub |
| 21 | paved_concrete | 67 | sandstone-soil | 104 | scrub (shaded) |
| 22 | pebbled_asphalt | 68 | sandstone_rock | 105 | scrub-grass-soil |
| 23 | pine_wood | 69 | sandy_loam | 106 | scrub-grass-soil (shaded) |
| 24 | red_brick | 70 | scrub-soil | 107 | tree_bark |
| 25 | roof_tar | 71 | scrub-soil (shaded) | 108 | tree_bark (shaded) |
| 26 | rusting_steel | 72 | silt-sand | 109 | tundra |
| 27 | urban_commercial | 73 | silty_clay | 110 | tundra (shaded) |
| 28 | urban_residential | 74 | silty_loam | | |
| 29 | wood_siding | 75 | tilled_soil | | |
| | PAINTS | 76 | varnished_sand | | |
| 30 | ash_grey | 77 | varnished_sandstone | | |
| 31 | battleship_grey | 78 | water | | |
| 32 | blackish_brown | 79 | wet_lakebed | | |
| 33 | bleached_yellow | 80 | wet_seabed | | |
| 34 | canary_yellow | 81 | wet_soil | | |
| 35 | dark_tan | 82 | white_sand | | |
| 36 | jet_black | | | | |
| 37 | kelly_green | | | | |
| 38 | light_red | | | | |
| 39 | light_tan | | | | |
| 40 | mint_green | | | | |
| 41 | mustard_yellow | | | | |
| 42 | off_white | | | | |
| 43 | olive_green | | | | |
| 44 | sky_blue | | | | |
| 45 | snow_white | | | | |

Table 2-1: List of materials tested in validation and associated material codes.

the fact that the level of errors associated with the SensorVision thermal emission model is highly dependent on the material emissivity.

Figure 2-2 shows the same results as those displayed in Figure 2-1 except that they have been transformed into the temperature domain. The exact and SensorVision computed radiance values are converted into effective temperatures, which are more intuitive to interpret. The effective temperature (T_{eff}) is defined as the temperature of a blackbody that would generate the same radiance (L) as that observed, as given by

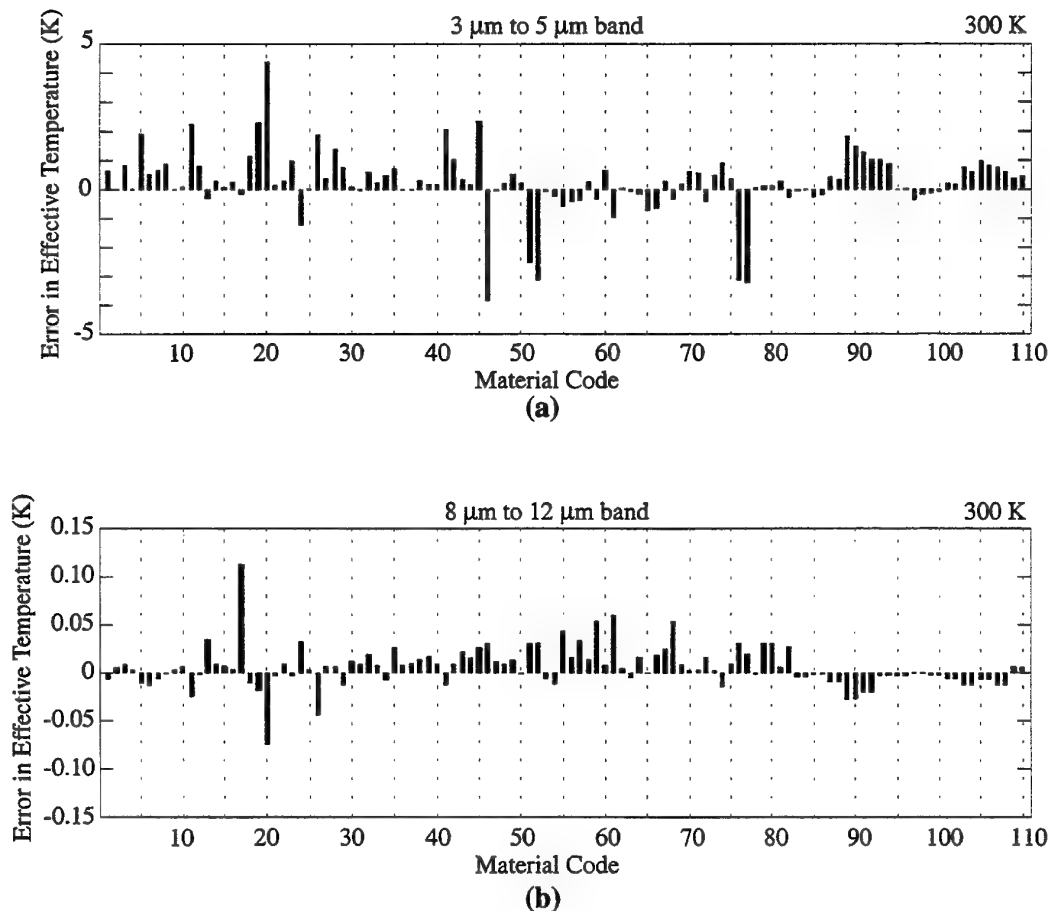


Figure 2-2: Bar graphs showing the error in effective temperature caused by the SensorVision thermal emission model as a function of material for (a) the MWIR band and (b) the LWIR band. The temperature is assumed to be 300 K and the atmospheric transmission coefficient is assigned a value of unity.

$$\int_{\lambda_1}^{\lambda_2} L_{\lambda}^{bb}(T_{eff}) d\lambda = L. \quad (2-18)$$

Function $L_{\lambda}^{bb}(T)$ is the blackbody equation (2-1). The errors in Figure 2-2 are expressed in terms of the difference in effective temperatures between the SensorVision generated results and the exact results.

It is important to understand that the SensorVision errors (expressed as percentage radiance error or effective temperature difference) due to the variability in the spectral emissivity data cannot be separated from the effect of variations in Planck's blackbody curve. Consequently, for greater insight, the second moment of the spectral emissivity data needs to be computed. Figure 2-3 shows the second moment values for the spectral

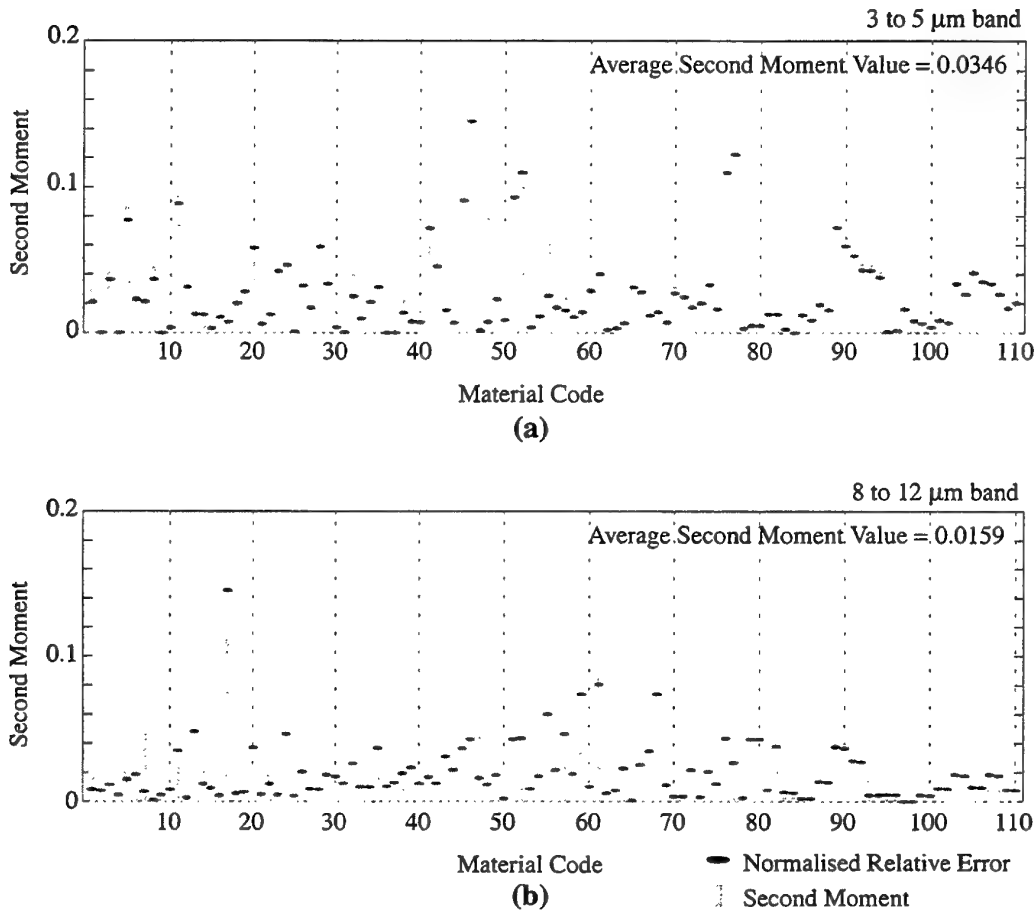


Figure 2-3: Bar graphs of second moments of material emissivities for (a) the MWIR band, and (b) the LWIR band.

emissivity data for the 110 materials considered. A second moment of zero corresponds to the best case where the emissivity is constant over the waveband, while a second moment of 0.5 corresponds to the worst case. In the worst case, the material's spectral emissivity has a value of one for exactly half of the waveband and zero for the other half. Overlaid on Figure 2-3(a) and Figure 2-3(b) are the relative error results from Figure 2-1(a) and Figure 2-1(b), respectively. These errors are normalised to enable a visual comparison with the second moment values, hence they are not associated with any y-axis scale. As can be observed in the bar graphs of Figure 2-3, the second moment does indeed provide a reasonable method of estimating the level of errors associated with the use of certain materials in SensorVision simulations. Furthermore, comparisons of Figure 2-3(a) and Figure 2-3(b) indicate that the material emissivity data tend to fluctuate less in the LWIR band compared to the MWIR band. This inference is further supported by an average second moment value of 0.0159 in the LWIR band compared to an average value of 0.0349 in the MWIR band. Note that the magnitude of improvement in the second moment value for the LWIR band compared to the MWIR band does not directly reflect the level of improvement in the relative errors (of Figure 2-1) or the effective temperature difference values (of Figure 2-2). The second moments computed in Figure 2-3 is dependent only on the spectral emissivity data, while the relative error (or the effective temperature difference) depends on both the spectral emissivity and the temperature. The relative error calculations, are biased by variations in the Planck's blackbody curve (see Section 2.5), and are therefore not good independent indicators of which materials cause SensorVision errors.

From the results of this validation, it is concluded that the SensorVision thermal emission model is more suited to LWIR simulations since materials tend to have spectral emissivity curves that fluctuate less in the 8 to 12 μm band compared to the 3 to 5 μm band. Given that the second moment has a maximum value of 0.5 and a minimum value of zero for emissivity data, a reasonable figure of merit or error indicator (EI) with a more intuitive range of zero to 100 can be defined as

$$EI_{\epsilon} = 100 \times 2e_{\epsilon} = 100 \times \frac{2}{N} \sum_{n=1}^N [\epsilon_{\lambda}(n) - \bar{\epsilon}]^2. \quad (2-19)$$

Table 2-2 lists the EI_{ϵ} values for the 110 materials currently in the SensorVision materials database. This table can be consulted when constructing SensorVision simulations in order to make competent decisions on whether certain materials should be included in the simulation.

| Code | Error Indicator (EI_{ϵ}) | | Code | Error Indicator (EI_{ϵ}) | | Code | Error Indicator (EI_{ϵ}) | |
|------|--|------|------|--|------|------|--|------|
| | MWIR | LWIR | | MWIR | LWIR | | MWIR | LWIR |
| 1 | 5.9 | 5.0 | 38 | 4.5 | 1.7 | 75 | 4.5 | 0.9 |
| 2 | 0.3 | 0.7 | 39 | 2.0 | 2.7 | 76 | 21.1 | 6.3 |
| 3 | 8.4 | 2.0 | 40 | 2.3 | 1.3 | 77 | 24.9 | 3.9 |
| 4 | 0.2 | 1.2 | 41 | 17.4 | 3.3 | 78 | 1.0 | 0.4 |
| 5 | 17.2 | 6.5 | 42 | 9.7 | 1.8 | 79 | 3.3 | 6.7 |
| 6 | 5.1 | 2.7 | 43 | 4.4 | 2.4 | 80 | 3.3 | 6.7 |
| 7 | 5.5 | 9.4 | 44 | 4.2 | 1.8 | 81 | 3.6 | 0.6 |
| 8 | 9.0 | 0.3 | 45 | 19.8 | 3.7 | 82 | 5.6 | 14.5 |
| 9 | 0.2 | 0.5 | 46 | 29.1 | 6.7 | 83 | 0.6 | 0.6 |
| 10 | 1.1 | 0.8 | 47 | 3.5 | 8.9 | 84 | 0 | 0.6 |
| 11 | 18.9 | 4.8 | 48 | 16.1 | 8.0 | 85 | 2.3 | 0.2 |
| 12 | 8.9 | 0.7 | 49 | 6.4 | 1.4 | 86 | 1.7 | 0.2 |
| 13 | 15.2 | 6.7 | 50 | 13.8 | 4.3 | 87 | 3.9 | 1.2 |
| 14 | 3.9 | 4.2 | 51 | 18.5 | 6.7 | 88 | 3.6 | 1.2 |
| 15 | 1.9 | 2.7 | 52 | 21.1 | 6.3 | 89 | 14.5 | 8.2 |
| 16 | 6.1 | 3.4 | 53 | 1.0 | 0.8 | 90 | 12.9 | 7.9 |
| 17 | 1.6 | 24.6 | 54 | 2.4 | 1.8 | 91 | 10.7 | 4.8 |
| 18 | 3.9 | 1.9 | 55 | 12.9 | 9.4 | 92 | 9.5 | 4.6 |
| 19 | 5.9 | 1.4 | 56 | 7.7 | 2.9 | 93 | 9.4 | 3.0 |
| 20 | 13.4 | 3.9 | 57 | 4.9 | 5.0 | 94 | 8.3 | 2.9 |
| 21 | 3.6 | 2.1 | 58 | 2.5 | 1.7 | 95 | 0.5 | 0.5 |
| 22 | 3.9 | 4.2 | 59 | 5.8 | 7.3 | 96 | 0.3 | 0.5 |
| 23 | 10.2 | 3.6 | 60 | 8.5 | 1.0 | 97 | 3.0 | 0 |
| 24 | 17.4 | 4.5 | 61 | 17.3 | 16.9 | 98 | 1.5 | 0 |
| 25 | 0.3 | 0.3 | 62 | 0.6 | 0.5 | 99 | 1.2 | 0.4 |
| 26 | 6.6 | 2.4 | 63 | 1.0 | 0.7 | 100 | 0.7 | 0.4 |
| 27 | 3.4 | 0.8 | 64 | 10.2 | 3.1 | 101 | 2.2 | 0.8 |
| 28 | 11.6 | 0.8 | 65 | 7.0 | 0.4 | 102 | 2.0 | 0.8 |
| 29 | 6.9 | 1.7 | 66 | 7.6 | 2.7 | 103 | 6.9 | 1.7 |
| 30 | 1.3 | 1.9 | 67 | 4.5 | 3.0 | 104 | 6.0 | 1.6 |
| 31 | 0.2 | 1.6 | 68 | 5.8 | 7.3 | 105 | 8.7 | 2.6 |
| 32 | 8.1 | 3.6 | 69 | 12.7 | 6.0 | 106 | 7.7 | 2.5 |
| 33 | 4.0 | 1.0 | 70 | 6.3 | 0.3 | 107 | 6.9 | 1.7 |
| 34 | 4.3 | 2.0 | 71 | 5.5 | 0.3 | 108 | 6.0 | 1.6 |
| 35 | 6.6 | 3.2 | 72 | 7.7 | 2.9 | 109 | 3.9 | 0.8 |
| 36 | 0.3 | 1.3 | 73 | 11.2 | 0.5 | 110 | 4.5 | 0.8 |
| 37 | 0.4 | 1.4 | 74 | 17.2 | 3.2 | | | |

Table 2-2: Emissivity error indicator values for materials.

2.4 Effect of Variability of Atmospheric Transmission Coefficient

In the validation described in Section 2.3, the atmospheric transmission coefficient was assumed to have a constant value of one and it was subsequently ignored. In this section, the effect of the spectral atmospheric transmission coefficient on the accuracy of the SensorVision thermal emission model will be assessed. The validation procedure used in this section is essentially the same as that employed in the previous section. The variability of the spectral transmission coefficient can be quantified by using the second moment, and an error indicator (EI) can be defined according to

$$EI_{\tau} = 100 \times \frac{2}{N} \sum_{n=1}^N [\tau_{\lambda}(n) - \bar{\tau}]^2. \quad (2-20)$$

Again, an EI value of zero represents the best case while a value of 100 indicates the worst case.

The atmospheric transmission coefficient is a complex parameter that is dependent on several factors including the weather conditions, the atmospheric profile, the waveband, and the LOS path between the sensor and the radiating material. It is a difficult parameter to predict due to its dependence on many influences. In this validation effort, a program called the MOSART (Moderate Spectral Atmospheric Radiance and Transmittance) code is used to generate the spectral atmospheric transmission coefficient for a range of different LOS paths for both the MWIR and LWIR bands. The transmission coefficients were computed for a location in northern Australia for the date 31st January 1998 at time 15:00 LST (local standard time) or 5:30 GMT (Greenwich Mean Time). The choice of these parameters was mainly arbitrary. The LOS paths for which the spectral transmission coefficients were computed are listed in Table 2-3, and included horizontal paths to 90° slant paths with ranges varying from 1 km to 50 km. In all cases, the altitude at the lower end of the path was 100 m. The computed EI values associated with the transmission coefficients for these paths are listed in Table 2-4. From Table 2-4, it is clear that the EI values are typically smaller in the LWIR band compared to the MWIR band. In fact, some of the EI values for the MWIR band are very large (with values in excess of 70 compared to a worst case value of 100) and indicate that the transmission coefficient varies significantly in the MWIR band. Scrutiny of Figure 2-4, which contains some atmospheric transmission coefficient plots, reveals the reasons for these observations. The variability of the transmission coefficient curve is clearly lower in the LWIR band compared to the MWIR band. In particular, there is a complete null at 4.3 μm due to CO₂ (carbon dioxide) absorption, which contributes to a large EI value in the MWIR band. The general decrease in EI values as the range increases is caused by the fact that the atmospheric attenuation increases with range. Consequently, the transmission coefficient is reduced and the variability in the spectral curve decreases. Figure 2-4(b)

shows a transmission coefficient plot for a high attenuation case resulting in lower variability in both the MWIR and LWIR cases, compared to Figure 2-4(a). As the elevation angle for the LOS path approaches 90 degrees, the effect of range becomes less pronounced due to the thinner atmosphere at higher altitudes. Furthermore, in the LWIR case, the introduction of some high altitude atmospheric molecular species has caused additional attenuation near 10 μm , which was not evident at lower altitudes (compare Figure 2-4(d) to Figure 2-4(c)). This extra attenuation at 10 μm increases the variability of the LWIR transmission coefficient and hence causes a slight increase in the EI values as the LOS path extends to higher altitudes.

The main conclusion drawn from the results contained in Table 2-4 is that the SensorVision thermal emission model is more suited to LWIR simulations than MWIR simulations. The large variations in the spectral atmospheric transmission coefficient in the MWIR band may introduce significant errors in the SensorVision simulation. However, the level of errors will reduce if narrower bands within the MWIR band are considered, especially if the null in the vicinity of 4.3 μm is omitted from the waveband.

In a HIL simulation, it is difficult to determine what type of LOS paths are likely to be encountered within the simulation. However, given that the engagement scenario is known prior to the simulation, the results contained within Table 2-4 will aid in the determination of the likely level of errors associated with different parts of the

| Code | Path Description | Range | Code | Path Description | Range |
|------|--------------------------|-------|------|--------------------------|-------|
| 1-1 | Horizontal Path | 1 km | 4-1 | Slant Path 30° Elevation | 1 km |
| 1-2 | | 2 km | 4-2 | | 2 km |
| 1-3 | | 5 km | 4-3 | | 5 km |
| 1-4 | | 10 km | 4-4 | | 10 km |
| 1-5 | | 20 km | 4-5 | | 20 km |
| 1-6 | | 50 km | 4-6 | | 50 km |
| 2-1 | Slant Path 10° Elevation | 1 km | 5-1 | Slant Path 60° Elevation | 1 km |
| 2-2 | | 2 km | 5-2 | | 2 km |
| 2-3 | | 5 km | 5-3 | | 5 km |
| 2-4 | | 10 km | 5-4 | | 10 km |
| 2-5 | | 20 km | 5-5 | | 20 km |
| 2-6 | | 50 km | 5-6 | | 50 km |
| 3-1 | Slant Path 20° Elevation | 1 km | 6-1 | Slant Path 90° Elevation | 1 km |
| 3-2 | | 2 km | 6-2 | | 2 km |
| 3-3 | | 5 km | 6-3 | | 5 km |
| 3-4 | | 10 km | 6-4 | | 10 km |
| 3-5 | | 20 km | 6-5 | | 20 km |
| 3-6 | | 50 km | 6-6 | | 50 km |

Table 2-3: List of LOS paths tested in validation of SensorVision thermal emission model.

| Code | Path Description | Range | Error Indicator | |
|------|--------------------------|-------|-----------------|------|
| | | | MWIR | LWIR |
| 1-1 | Horizontal Path | 1 km | 71.3 | 27.8 |
| 1-2 | | 2 km | 68.9 | 28.0 |
| 1-3 | | 5 km | 57.7 | 18.8 |
| 1-4 | | 10 km | 42.3 | 7.0 |
| 1-5 | | 20 km | 24.0 | 0.8 |
| 1-6 | | 50 km | 5.4 | 0 |
| 2-1 | Slant Path 10° Elevation | 1 km | 71.3 | 27.6 |
| 2-2 | | 2 km | 69.2 | 28.2 |
| 2-3 | | 5 km | 59.7 | 22.1 |
| 2-4 | | 10 km | 49.2 | 14.3 |
| 2-5 | | 20 km | 41.6 | 10.1 |
| 2-6 | | 50 km | 35.8 | 8.7 |
| 3-1 | Slant Path 20° Elevation | 1 km | 71.3 | 27.5 |
| 3-2 | | 2 km | 69.4 | 28.4 |
| 3-3 | | 5 km | 62.0 | 24.5 |
| 3-4 | | 10 km | 56.4 | 21.3 |
| 3-5 | | 20 km | 52.2 | 19.9 |
| 3-6 | | 50 km | 49.3 | 19.2 |
| 4-1 | Slant Path 30° Elevation | 1 km | 71.2 | 27.4 |
| 4-2 | | 2 km | 69.6 | 28.4 |
| 4-3 | | 5 km | 64.2 | 26.3 |
| 4-4 | | 10 km | 60.5 | 25.1 |
| 4-5 | | 20 km | 57.6 | 24.2 |
| 4-6 | | 50 km | 56.2 | 24.6 |
| 5-1 | Slant Path 60° Elevation | 1 km | 71.1 | 27.0 |
| 5-2 | | 2 km | 70.2 | 28.4 |
| 5-3 | | 5 km | 67.5 | 28.4 |
| 5-4 | | 10 km | 65.4 | 28.0 |
| 5-5 | | 20 km | 64.2 | 27.7 |
| 5-6 | | 50 km | 63.9 | 29.3 |
| 6-1 | Slant Path 90° Elevation | 1 km | 71.1 | 26.9 |
| 6-2 | | 2 km | 70.4 | 28.4 |
| 6-3 | | 5 km | 68.2 | 28.6 |
| 6-4 | | 10 km | 66.5 | 28.3 |
| 6-5 | | 20 km | 65.6 | 28.3 |
| 6-6 | | 50 km | 65.4 | 29.9 |

Table 2-4: Error indicator values for LOS paths tested.

engagement. For example, consider an air to ground scenario where a weapon is launched from an air platform at a range of 10 km. Say the weapon has a MWIR seeker and the engagement is such that the trajectory of the missile follows an approximately straight path with an elevation of approximately 10° . From the EI values listed in Table 2-4, it is expected that SensorVision generated scenes will have errors associated with the thermal emission model that are moderate at the start of the engagement (EI value of around 49). These errors become progressively worse (EI value approaching 71) as the missile homes in on the target. Actual errors will also depend on the material composition and temperature of the target.

Having analysed the variability of material emissivities and atmospheric transmission coefficients independently, the next question that needs to be answered is the effect of both parameters on the SensorVision thermal emission model. In essence, it is necessary to determine the variability of the product of the emissivity and transmission coefficient

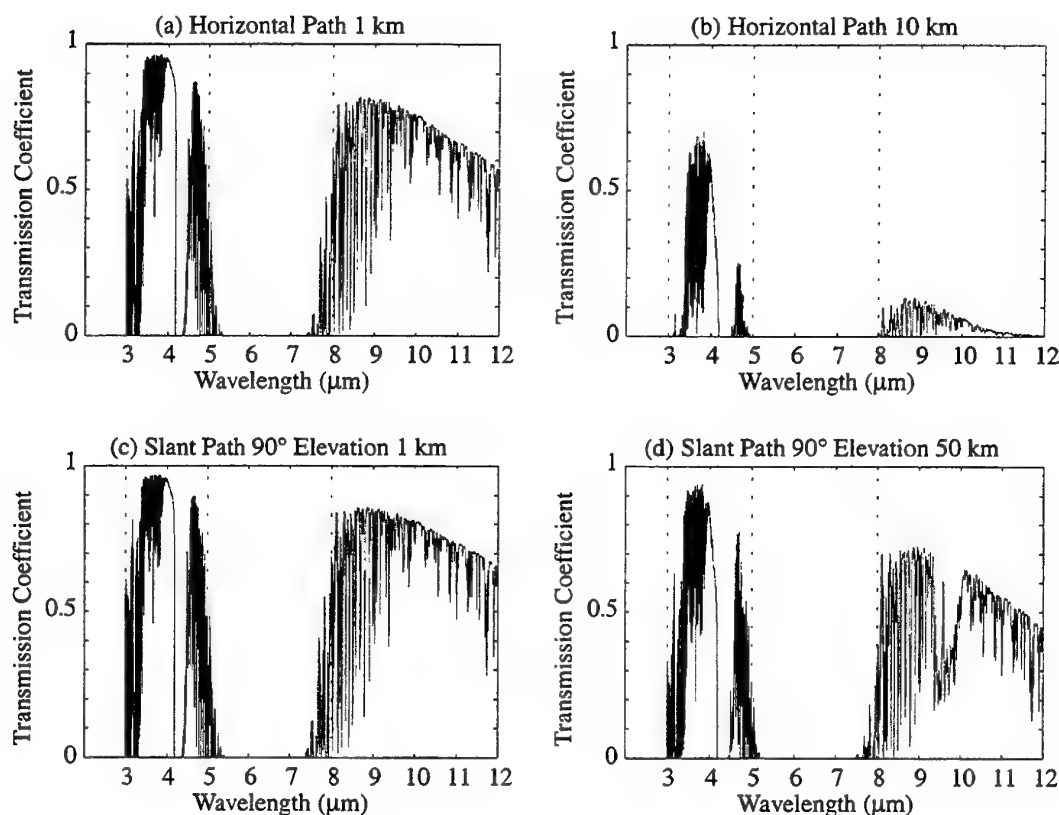


Figure 2-4: Plot of atmospheric transmission coefficient as a function of wavelength for a selection of LOS paths: (a) a horizontal 1 km path; (b) a horizontal 10 km path; (c) a vertical 1 km path; and (d) a vertical 50 km path.

parameters. A simple and quick method of combining the second moments of the emissivity and transmission coefficient is to apply

$$e_{\varepsilon\tau} \cong \bar{\varepsilon}\bar{\tau} \sqrt{\left(\frac{e_{\varepsilon}}{\bar{\varepsilon}}\right)^2 + \left(\frac{e_{\tau}}{\bar{\tau}}\right)^2}. \quad (2-21)$$

Parameter $e_{\varepsilon\tau}$ is the second moment value of the emissivity and transmission coefficient product, e_{τ} and $\bar{\tau}$ are the second moment and mean of the transmission coefficient, respectively, and e_{ε} and $\bar{\varepsilon}$ are the second moment and mean of the emissivity, respectively. Equation (2-21) is a formula used to calculate errors in measurements due to multiplication operations. It is only an approximate formula but it should be sufficiently accurate for establishing guidelines in the SensorVision validation. The application of (2-21) is easier than directly computing the second moment of the emissivity and transmission coefficient product. An appropriate error indicator for the product can be defined as

$$EI_{\varepsilon\tau} = 100 \times 2e_{\varepsilon\tau}. \quad (2-22)$$

The error between the exact equation and the SensorVision thermal emission model was calculated for all 110 materials listed in Table 2-1 and the 36 LOS paths listed in Table 2-3. A surface temperature of 300 K was again assumed, and both the MWIR and LWIR bands were considered. The resultant data set contained 7920 values, which is too much information to present in this report. Table 2-5 summarises the results by displaying the statistics of the data set for each LOS path. As evident in these results, errors associated with the MWIR band are significant. Average relative errors are 12.5% for a range of 1 km and increase to a value of 83.8% for a range of 50 km assuming a horizontal LOS path. Note that the large value of 83.8% for the 50 km range is caused by the effect of the transmission coefficient on the calculated radiances. High attenuation causes the exact radiance to be small and the calculated relative error is amplified due to the quotient operation in (2-17). For this reason, the relative error values can be misleading and the errors expressed as effective temperatures may provide a better indication of the inaccuracies associated with the SensorVision thermal emission model. Again, it is emphasised that the actual values contained in Table 2-5 should only be considered, keeping in mind that a surface temperature of 300 K has been assumed. As will be explained in the next section, the chosen temperature of 300 K amplifies any errors associated with the MWIR band while reducing errors associated with the LWIR band. The EI values contained in Table 2-2 and Table 2-4 are more reliable in the formulation of conclusions than the results listed in Table 2-5. Furthermore, using EI values is much easier and quicker than performing the laborious task of calculating relative errors or effective temperature differences.

| Path Code | LWIR Band | | | | | | MWIR Band | | | | | |
|-----------|-------------------|-------------------|-------------------|-------------------|-------------------|-------------------|-------------------|-------------------|-------------------|-------------------|-------------------|-------------------|
| | Minimum | | Maximum | | Average | | Minimum | | Maximum | | Average | |
| | ΔL (%) | ΔT (K) | ΔL (%) | ΔT (K) | ΔL (%) | ΔT (K) | ΔL (%) | ΔT (K) | ΔL (%) | ΔT (K) | ΔL (%) | ΔT (K) |
| 1-1 | 0.7 | 0.2 | 33.0 | 5.5 | 12.5 | 2.8 | -1.5 | -0.5 | 0.7 | 0.3 | -0.3 | -0.2 |
| 1-2 | 12.3 | 2.6 | 40.5 | 6.3 | 21.1 | 4.3 | -2.5 | -0.7 | 1.6 | 0.7 | -0.5 | -0.2 |
| 1-3 | 33.3 | 6.1 | 55.9 | 8.0 | 39.1 | 7.0 | -5.1 | -0.9 | 4.5 | 1.4 | -0.9 | -0.3 |
| 1-4 | 48.7 | 7.4 | 70.1 | 10.1 | 56.2 | 8.7 | -8.0 | -0.7 | 9.0 | 1.4 | -1.2 | -0.2 |
| 1-5 | 62.3 | 7.8 | 95.6 | 11.2 | 72.3 | 9.4 | -10.5 | -0.1 | 15.6 | 0.2 | -1.2 | -0.0 |
| 1-6 | 71.1 | 5.4 | 118 | 10.3 | 83.8 | 8.3 | -12.5 | -0.0 | 26.7 | 0.0 | -0.7 | -0.0 |
| 2-1 | 0.2 | 0.1 | 32.7 | 5.5 | 12.1 | 2.7 | -1.4 | -0.4 | 0.6 | 0.3 | -0.3 | -0.2 |
| 2-2 | 10.6 | 2.3 | 39.5 | 6.2 | 19.8 | 4.1 | -2.3 | -0.7 | 1.3 | 0.6 | -0.5 | -0.2 |
| 2-3 | 29.3 | 5.4 | 52.2 | 7.4 | 34.6 | 6.4 | -4.2 | -0.9 | 3.3 | 1.1 | -0.8 | -0.3 |
| 2-4 | 40.7 | 6.8 | 62.8 | 9.0 | 47.2 | 7.8 | -5.9 | -0.8 | 5.5 | 1.5 | -1.1 | -0.3 |
| 2-5 | 50.3 | 7.5 | 71.4 | 10.1 | 57.4 | 8.8 | -6.8 | -0.8 | 7.0 | 1.5 | -1.1 | -0.3 |
| 2-6 | 58.8 | 8.0 | 81.0 | 10.9 | 66.1 | 9.5 | -6.6 | -0.7 | 7.4 | 1.4 | -1.1 | -0.2 |
| 3-1 | -0.2 | -0.1 | 32.4 | 5.4 | 11.8 | 2.6 | -1.3 | -0.4 | 0.6 | 0.3 | -0.3 | -0.1 |
| 3-2 | 9.1 | 2.0 | 38.6 | 6.1 | 18.8 | 3.9 | -2.1 | -0.6 | 1.2 | 0.5 | -0.5 | -0.2 |
| 3-3 | 25.3 | 4.7 | 49.3 | 7.2 | 31.2 | 5.9 | -3.5 | -0.9 | 2.5 | 0.9 | -0.7 | -0.3 |
| 3-4 | 33.7 | 6.1 | 56.3 | 7.9 | 39.3 | 6.9 | -4.2 | -0.9 | 3.3 | 1.1 | -0.8 | -0.3 |
| 3-5 | 38.5 | 6.6 | 60.8 | 8.5 | 44.3 | 7.5 | -4.2 | -0.8 | 3.4 | 1.1 | -0.8 | -0.3 |
| 3-6 | 41.3 | 6.8 | 63.4 | 8.8 | 47.1 | 7.8 | -3.8 | -0.7 | 3.3 | 1.0 | -0.7 | -0.2 |
| 4-1 | -0.6 | -0.1 | 32.1 | 5.4 | 11.5 | 2.6 | -1.3 | -0.4 | 0.5 | 0.3 | -0.3 | -0.1 |
| 4-2 | 7.9 | 1.7 | 37.8 | 6.0 | 17.9 | 3.8 | -2.0 | -0.6 | 1.0 | 0.5 | -0.4 | -0.2 |
| 4-3 | 21.4 | 4.1 | 46.8 | 6.9 | 28.2 | 5.5 | -3.0 | -0.8 | 2.0 | 0.8 | -0.6 | -0.3 |
| 4-4 | 27.6 | 5.1 | 51.4 | 7.3 | 33.3 | 6.2 | -3.1 | -0.8 | 2.1 | 0.8 | -0.7 | -0.3 |
| 4-5 | 31.1 | 5.5 | 54.1 | 7.6 | 36.2 | 6.6 | -3.0 | -0.7 | 2.1 | 0.8 | -0.6 | -0.2 |
| 4-6 | 33.3 | 5.9 | 56.1 | 7.7 | 38.5 | 6.9 | -2.3 | -0.5 | 2.0 | 0.7 | -0.4 | -0.2 |
| 5-1 | -1.5 | -0.3 | 31.6 | 5.3 | 10.8 | 2.4 | -1.2 | -0.4 | 0.5 | 0.2 | -0.3 | -0.1 |
| 5-2 | 5.5 | 1.2 | 36.3 | 5.9 | 16.1 | 3.5 | -1.7 | -0.5 | 0.8 | 0.4 | -0.4 | -0.2 |
| 5-3 | 13.5 | 2.8 | 41.7 | 6.5 | 22.2 | 4.5 | -2.0 | -0.6 | 1.1 | 0.5 | -0.5 | -0.2 |
| 5-4 | 16.6 | 3.3 | 44.1 | 6.7 | 24.7 | 4.9 | -2.0 | -0.6 | 1.0 | 0.4 | -0.4 | -0.2 |
| 5-5 | 17.7 | 3.5 | 45.1 | 6.8 | 25.7 | 5.1 | -1.8 | -0.5 | 0.9 | 0.4 | -0.4 | -0.2 |
| 5-6 | 19.7 | 3.8 | 46.6 | 7.0 | 27.4 | 5.4 | -1.2 | -0.3 | 0.8 | 0.3 | -0.2 | -0.1 |
| 6-1 | -1.7 | -0.4 | 31.4 | 5.3 | 10.6 | 2.4 | -1.2 | -0.4 | 0.4 | 0.2 | -0.3 | -0.1 |
| 6-2 | 4.8 | 1.1 | 35.8 | 5.8 | 15.6 | 3.4 | -1.6 | -0.5 | 0.8 | 0.4 | -0.4 | -0.2 |
| 6-3 | 11.3 | 2.4 | 40.4 | 6.3 | 20.6 | 4.3 | -1.8 | -0.5 | 0.9 | 0.4 | -0.4 | -0.2 |
| 6-4 | 13.7 | 2.8 | 42.4 | 6.5 | 22.7 | 4.6 | -1.7 | -0.5 | 0.8 | 0.4 | -0.4 | -0.2 |
| 6-5 | 14.7 | 3.0 | 43.1 | 6.6 | 23.5 | 4.7 | -1.5 | -0.4 | 0.7 | 0.3 | -0.3 | -0.2 |
| 6-6 | 16.3 | 3.3 | 44.4 | 6.7 | 24.8 | 5.0 | -1.0 | -0.3 | 0.6 | 0.3 | -0.2 | -0.1 |

Table 2-5: Summary of errors generated by SensorVision thermal emission model including both material emissivity and atmospheric transmission coefficient data. Errors are represented in terms of percentage error (ΔL) relative to the exact radiance, and the difference (ΔT) between SensorVision and exact effective temperatures.

2.5 Effect of Variability of Planck's Blackbody Curve

Planck's blackbody equation (given by (2-1)) is a well known function, which has a temperature dependence. Figure 2-5 contains plots of Planck's curves as functions of temperature. As evident in these plots, the peak of Planck's curve moves to the shorter wavelengths and increases in magnitude as the temperature is raised.

The variability of Planck's blackbody curve within the waveband of interest has an impact on the errors associated with the SensorVision thermal emission model. Even though the variations in the emissivity and transmission coefficient parameters are the actual source of errors, the variability of Planck's curve substantially affects the error magnitudes. This statement is supported by the plots shown in Figure 2-6. In Figure 2-6, the mean relative error of the SensorVision thermal emission model is plotted as a function of temperature. The mean relative error is computed by calculating (2-17) for the 110 materials in the materials database, applying a modulus function to remove any sign dependence, and determining the mean over all materials. Note that the atmospheric transmission coefficient is assumed to have a value of one to simplify the calculations.

Figure 2-7 contains a plot of the EI values associated with the variability of Planck's blackbody curve in the waveband of interest. The EI value is calculated using

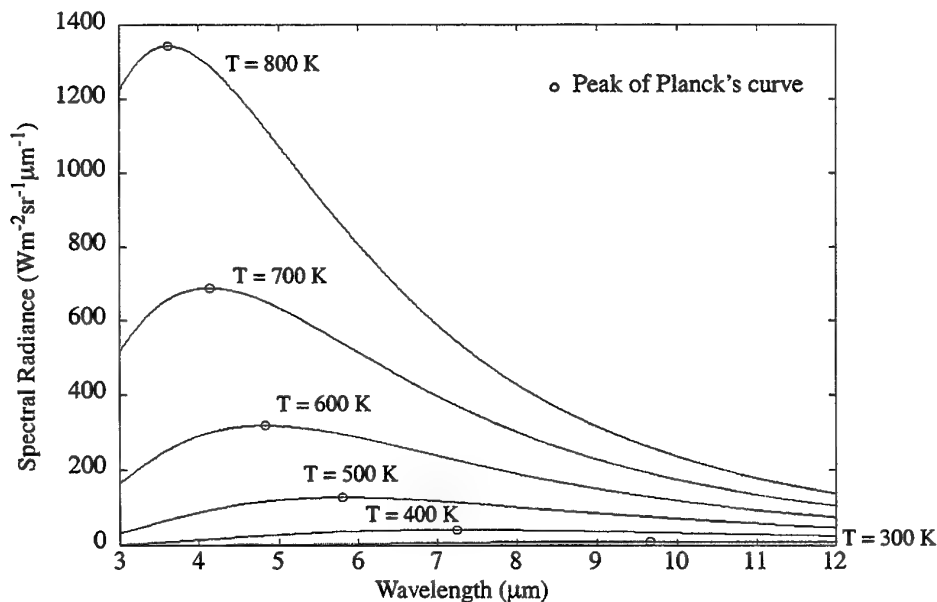


Figure 2-5: Plot of Planck's blackbody curves as a function of temperature.

$$EI_{bb} = 100 \times 2 \sqrt{\frac{\int_{\lambda_1}^{\lambda_2} (Ln_{\lambda}^{bb} - \overline{Ln}^{bb})^2 d\lambda}{(\lambda_2 - \lambda_1)}}, \quad (2-23)$$

where Ln_{λ}^{bb} is the Planck's blackbody curve normalised by its maximum value in the waveband of interest. Normalisation is required to limit Ln_{λ}^{bb} to values between zero and one, and ensure the EI value remains in the range zero to 100.

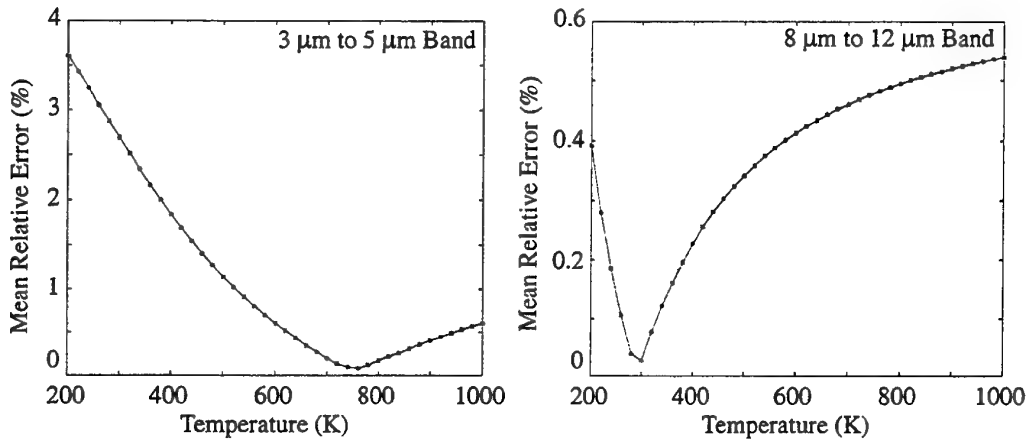


Figure 2-6: Mean relative error between SensorVision thermal emission model and exact model as a function of temperature. Atmospheric transmission coefficient is assumed to be unity and all 110 materials are included in the computation of the mean relative error.

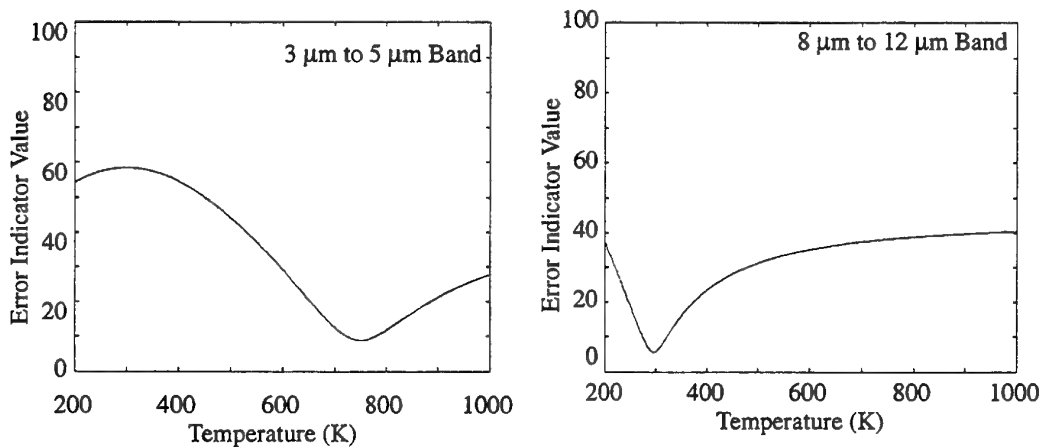


Figure 2-7: Plot of error indicator value of Planck's blackbody curve in waveband of interest as a function of temperature.

The key feature to note in Figure 2-6 and Figure 2-7 is the similarity between the curves. Clearly, the variability of the Planck's curve in the waveband of interest (quantified by the EI value) has an effect on the SensorVision errors. Furthermore, the effect appears to be linear in nature (at least in the temperature range 300 K to 1000 K). The minimum value of the EI parameter in the MWIR and LWIR bands correspond to the temperatures of 740.2 K and 293.7 K, respectively. This result is significant because materials used in simulations tend to have temperatures near ambient air temperature, which is near the optimal⁵ temperature for the LWIR band. Again, it appears that the SensorVision thermal emission model is more suited to LWIR simulations. However, simulations involving hot bodies (such as hot plumes and hot engine parts in air engagements) may result in greater errors in the LWIR band compared to the MWIR band. For instance, at a temperature of 700 K, the EI value in the MWIR band is 12.6 compared to 37.3 in the LWIR band. The mean relative error at 700 K (as plotted in Figure 2-6) is 0.2% in the MWIR band compared to 0.46% in the LWIR band.

Due to the apparent linear relationship between the SensorVision thermal emission errors and the EI values for the Planck's blackbody curves, a total error indicator value can be estimated by applying

$$EI_{total} = \frac{EI_{\epsilon\tau}}{100} \times EI_{bb}. \quad (2-24)$$

The error indicator value $EI_{\epsilon\tau}$ is given by (2-22) and EI_{bb} is given by (2-23). The total EI value is again limited to the range zero to 100, where a value of 100 corresponds to the worst possible case. Again, the concept behind the EI value is to aid users in the construction of SensorVision simulations for HIL testing.

2.6 Chapter Summary

In this chapter, the SensorVision thermal emission model (as applied to solid opaque Lambertian scene materials) was validated. The validation involved determining the level of errors associated with the application of the SensorVision approximation whereby spectral terms are moved outside of the spectral integration and replaced by their in-band averaged values. The two spectral terms affected were the material's spectral emissivity and the spectral atmospheric transmission coefficient. The effect of moving each of these parameters outside of the integration was determined independently and a figure of merit referred to as the error indicator (EI) was proposed. The development of the EI was one of the significant outcomes of this validation effort. The total combined EI value, given by (2-4), strongly reflects the error magnitude

⁵. The temperature is optimal in the sense that it minimises the errors associated with the SensorVision thermal emission model.

associated with the SensorVision thermal emission model, and it can be determined much quicker than the direct computation of the actual error. The error indicator should be used in the construction phase of a HIL simulation to identify situations and scenarios whereby the performance of SensorVision, in producing thermal emission signature components, may be deficient.

It was concluded from the validation effort that the SensorVision thermal emission model is more suited to LWIR simulations. The reasons for this conclusion are three-fold:

- spectral emissivities of many materials tend to have lower variability in the LWIR band compared to the MWIR band;
- the spectral atmospheric transmission coefficient does not fluctuate significantly in the LWIR band; and
- the optimal temperature in the LWIR band corresponds to a value near ambient air temperature and objects in simulations tend to have temperatures near ambient.

The validation effort has shown that significant errors can be generated by the SensorVision thermal emission model, especially for the MWIR case. However, this statement does not necessary preclude the use of SensorVision in MWIR simulations since the actual level of errors is strongly dependent on the materials, engagement scenarios, and actual waveband employed in the simulation. It is possible to minimise SensorVision related errors by carefully constructing simulations using the EI as a guide. Appendix A contains a summary explaining the use of EI values during simulation construction.

3. Validation of the Temperature Prediction Model¹

In the previous chapter, the SensorVision thermal emission model was validated assuming the surface temperatures of the materials were known. In this chapter, the temperature prediction model employed by SensorVision will be experimentally validated against empirical data.

3.1 The SensorVision Temperature Prediction Model

SensorVision comprises a software library and two database construction tools, called the MATTM (MOSART Atmospheric Tool) and the TMMTM (Texture Material Mapper). The software library performs the real-time radiometric calculations and provides Vega with the required functionality to render IR scenes. Both database construction tools are used in preprocessing operations prior to the real-time simulation. The purpose of the TMM utility is to allow the user to assign material properties (reflectance) to textures, which are pasted on object models. The MAT generates databases for atmospheric quantities and surface temperatures of scene materials. This chapter focuses on the MAT since it is the SensorVision component responsible for computing material surface temperatures.

The MAT is essentially a SensorVision interface for the MOSART² (Moderate Spectral Atmospheric Radiance and Transmittance) code. The MAT takes a user input file, executes the MOSART program, and records the MOSART output results into database files with the format required by SensorVision. Consequently, the validation effort described in this chapter is essentially a validation of the temperature prediction model employed by the MOSART code with the addition of the MAT interface. The component of the MOSART program that performs the surface temperature computations is called the TERTEM (Terrain Temperatures) code. The TERTEM algorithm uses a one-dimensional three-layer thermal model [4], consisting of a surface layer and two sub-layers. The surface material has some prescribed thickness and is represented by six heat transfer parameters: solar absorption, thermal emittance, thermal conductance, specific heat, density, and characteristic length. Both sub-layers are assigned a material type with the first sub-layer given a thickness property. The second sub-layer is assumed to be infinite in depth. The TERTEM algorithm takes into account four heat transfer fluxes: radiation, convection, conduction, and evaporation. Radiation inputs are from only the sun and the sky. Effects of varying air temperature and humidity throughout the day are considered, but the wind speed and moisture content of materials are

¹ Most of the contents in this chapter have already been reported in reference [3]. It has been included in this report for the sake of completeness.

² MOSART is a U.S. Government standard atmospheric code developed by Phillips Laboratory, Department of Geophysics, Air Force Material Command, Hanscom AFB, Massachusetts.

assumed to be constant. Also, due to the one-dimensional model, any lateral transfer of heat is neglected. The TERTEM program should yield accurate results for most natural and man-made surfaces (such as soils, rocks, low-cropped vegetation, asphalt, and concrete). However, it cannot accurately model high vertical vegetation (such as trees) due to the dominant effect of lateral heat transfer processes, or operated vehicles (such as tanks, and aeroplanes) due to the significant influences of internal heat sources on surface temperatures.

The SensorVision predicted temperature results used in this validation effort were obtained directly from the MAT. The MAT input file allows the user to specify the atmospheric states, the spectral bands of interest with sensor spectral responses, and the range of material surface and observer geometries expected in the simulation. Heat transfer parameters for materials can also be modified by the user. Table 3-1 contains the list of material heat transfer parameters that can be adjusted by the user, while Table 3-2 contains the list of the MAT user input parameters. Once the MAT program is executed, three output files are generated: a file containing databases of solar atmospheric quantities (with parameters representing solar radiance, skyshine radiance, atmospheric path radiance, and atmospheric path transmission); a file containing databases of lunar atmospheric quantities (with parameters representing lunar radiance, emitted and skyshine radiance, emitted and scattered atmospheric path radiance, and atmospheric path transmission); and a file containing the database of predicted surface temperatures. Only the last output file is of interest in this report since it contains the MAT (and the MOSART code) predicted surface temperatures for the user-chosen materials given some specified geographical location, atmospheric state, and spectral band.

| Heat Transfer Parameter |
|-------------------------|
| Label |
| Default Material |
| Solar Absorptivity |
| Thermal Emissivity |
| Characteristic Length |
| Evaporation Index |
| Specific Heat |
| Thermal Conductivity |
| Density |
| Surface Layer Thickness |
| Sub-layer 1 Thickness |
| Sub-layer 1 Material |
| Sub-layer 2 Material |

Table 3-1: List of heat transfer parameters.

In this chapter, the SensorVision temperature prediction models are validated by comparing the MAT generated results against measured temperatures. This type of strategy can be described as a functional and experimental validation. The term functional refers to the fact that the physics of the model are not considered, rather only the model outputs are validated. The term experimental describes the fact that empirical data is used to validate the model. The measured data used in the validation were collected in trials at a location in northern Australia. The air temperature and the temperature of a concrete sample were recorded over a period of three years to enable

| MAT Input File Parameters | |
|--------------------------------|---|
| Atmospheric States | Latitude, Longitude (°) Year, Month, Day Model Atmosphere Name (e.g. TROPICAL_SUMMER) Temperature (Cold, Mean, Hot) Humidity (Dry, Mean, Wet) Wind (Calm, Mean, Windy) Cloud Cover (Clear, Cloudy) Cloud Base Altitude (km) Visibility Range (km) |
| Spectral Bands | Spectral Resolution (cm^{-1}) Number of Spectral Response Pairs (For each spectral response pair) Wavelength (mm), Response |
| Material Parameters | Number of Materials Material Names Number of Surface Altitudes Surface Altitudes (km) Number of Surface Orientation Azimuths Azimuths (°) Number of Surface Orientation Slopes Slopes (°) Number of Times Times (hours in local standard time) |
| Observer and Source Parameters | Number of LOS (Line of Sight) Ranges LOS Ranges (km) Number of Observer Altitudes Altitudes (km) Number of LOS elevations LOS elevations (°) Number of Solar/Lunar Elevations Elevations (°) Number of Solar/Lunar to Observer Azimuths Azimuths (°) |

Table 3-2: List of the MAT input file parameters.

the monthly averages of the daily temperature profiles to be determined. SensorVision generated temperature profiles were then compared with the monthly averages to determine the accuracy of the temperature prediction model. All simulations were run using version 3.1.1 of the MAT (packaged with SensorVision version 3.4.1.4, and Vega version 3.4), on an Onyx2™ SGI machine with operating system IRIX™ 6.5. The version of the MOSART code employed by SensorVision is not known, and there is the possibility that the MOSART code has been modified by the SensorVision developers.

3.2 Processing of Experimental Data

The measured temperature data were collected in 1991, 1992, and 1993, during an experimental trial with a purpose unrelated to the SensorVision validation effort. During these trials, thermal sensors were used to automatically record the air temperature and the temperature of a concrete sample at a location in northern Australia. The concrete specimen was a 350 mm layer of Portland cement on top of a 150 mm layer of gravel. Two temperature sensors were buried in 1 inch holes drilled into the surface of the concrete sample at different spatial locations. The holes were refilled with mortar. One air temperature and two concrete surface temperature readings were simultaneously recorded every 10 minutes throughout each 24-hour day. Data were collected for every month of the year, except December. However, not every month of each year or every day of each month was represented in the sample set. Table 3-3 lists the days in which some data were collected.

Before the experimental data could be compared against SensorVision generated results, some filtering was required to remove any data sets that were considered to be unreliable or erroneous. A temperature reading that is affected by a thermal sensor malfunction or is an anomalous measurement due to abnormal conditions is referred to as an outlier. Whenever an outlier was identified within a data set, the entire data set was removed from the sample space in order to reduce the complexity of the statistics calculations. In addition, incomplete data sets containing measurements for only part of the day were also removed from the sample space.

Figure 3-1(a) shows plots of the raw diurnal air and concrete temperature profiles for the 30 days of April over the years 1991 to 1993. As evident in the raw data plots for the concrete sample, several data sets are clearly erroneous. For example, several data sets contain negative temperature readings, which are improbable given the tropical climate of northern Australia. In comparison, very few data sets in the air temperature profiles contain obvious outliers.

Scrutiny of the concrete diurnal temperature profiles revealed that there were two types of obvious outliers associated with sensor malfunctions. A temperature of 99.9 °C was recorded when a failure in the thermal sensor occurred, while a large temperature

variation between consecutive temperature readings indicated a DC (direct current) bias problem within the sensor. Both outlier types were easily identified and the data sets containing these outliers were removed from the sample space. The identification of other outlier types was difficult due to an incomplete knowledge of the sensor characteristics, the measurement process, and the conditions under which each temperature reading was recorded. It was not easy to determine if a peculiar feature of a temperature profile was due to an erroneous measurement or due to a valid environmental condition. The only information that could be used in the detection of non-obvious outliers was the fact that three temperature readings (one air temperature and two concrete temperatures) were recorded simultaneously. All three diurnal

| | 1991 | 1992 | 1993 |
|-----------|-------------------|-----------------------------|--------------------|
| January | | 30, 31 (2 days) | |
| February | | 1, 4, 5, 18, 19 (5 days) | 12-28 (17 days) |
| March | 26-31 (6 days) | 2-31 (30 days) | 1-31 (31 days) |
| April | 1-30 (30 days) | 1-30 (30 days) | 1-30 (30 days) |
| May | 1-31 (31 days) | 1-31 (31 days) | 1-31 (31 days) |
| June | 1-30 (30 days) | 1-30 (30 days) | 1-30 (30 days) |
| July | 1-31 (31 days) | 1-31 (31 days) | 1-31 (31 days) |
| August | 1-31 (31 days) | 1-31 (31 days) | 1-31 (31 days) |
| September | 1-30 (30 days) | 1-30 (30 days) | 1-26 (26 days) |
| October | 1-31 (31 days) | 1-26, 28-31 (30 days) | |
| November | 1-11 (11 days) | 1-9, 12-30 (28 days) | |
| December | | | |

Table 3-3: List of days during 1991, 1992, and 1993 in which some temperature measurements were recorded.

temperature profiles, associated with a particular day and data set, should be reasonably well correlated because they were all measured under identical environmental conditions. In particular, the two concrete temperature profiles recorded during any day should have a high degree of correlation. An outlier can therefore be recognised as a temperature profile feature that is not mimicked in the other two temperature profiles measured during that same day. The three diurnal temperature profiles were plotted and compared for all data sets, and the identification of outliers (by a human operator) was

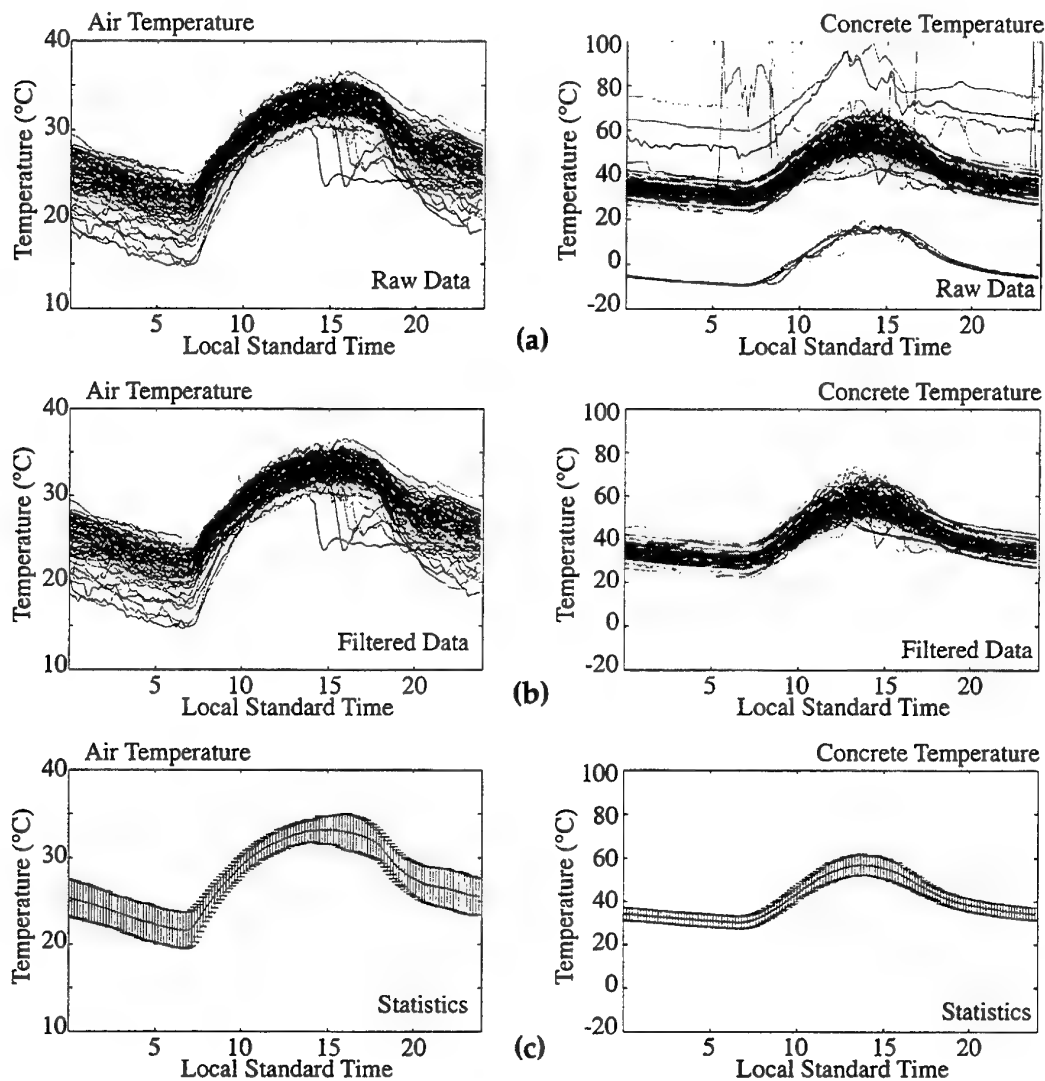


Figure 3-1: Plots of the (a) raw, (b) filtered, and (c) the statistics of the data sample space for measured air and concrete daily temperature profiles for the month of April (1991, 1992, and 1993). The data statistics are plotted as error bars with a mean and an error of one standard deviation.

performed. The process was subjective and conducted with the policy that only data sets with features that were blatant outliers were discarded. Figure 3-2 contains examples of diurnal temperature variations for two days. Figure 3-2(a) shows temperature profiles in which no outliers were identified, and Figure 3-2(b) shows an example of an outlier feature. In the first case, all three plots are well correlated while in the second case, the dashed line contains a spike near 4 p.m. that is not evident in the other two temperature profiles. The data set corresponding to the dashed line in Figure 3-2(b) was removed from the sample space. Note that the sudden decrease in temperature observed near 3 p.m. in Figure 3-2(b) may have been misinterpreted as an outlier if each temperature profile was individually scrutinized. However, because all three temperature profiles measured that day exhibited the same feature, it must be concluded that some valid environmental effect (such as a cool change or sudden rainfall) caused the rapid decrease in temperature.

Table 3-4 lists the total number of raw data sets, the number of data sets rejected on the basis that the records were incomplete or contained outliers, and the final sample space size for each month (combining the 1991, 1992, and 1993 data). Note that the large numbers of rejected data sets in the concrete sample space is mainly due to temperature readings that indicated sensor malfunctions. The embedding of the thermal sensors into the concrete sample caused a reduction in the reliability of the sensors. With reference to Table 3-4, the final sample space size for January is too small to be useable, hence January was not considered during the validation procedure. The number of data sets for

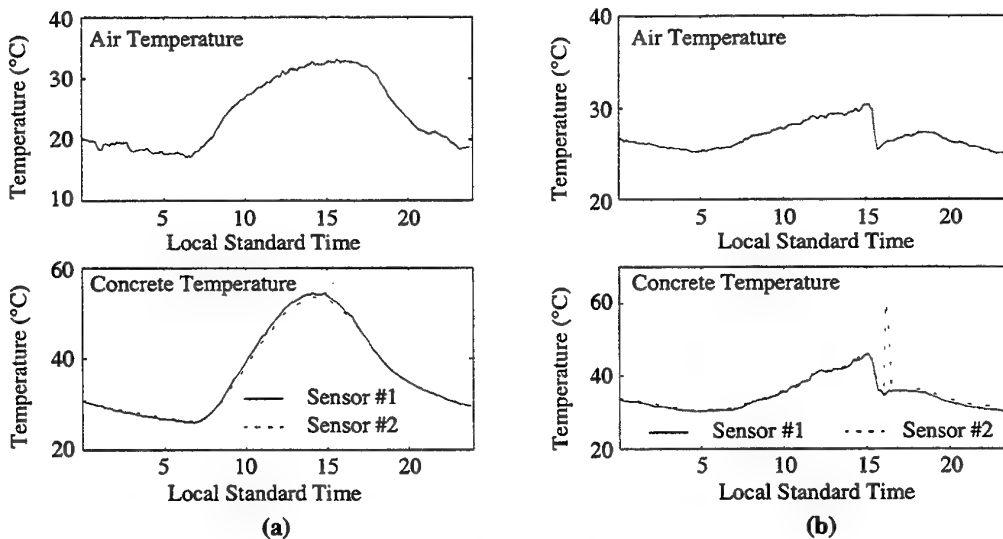


Figure 3-2: Examples of the temperature profile comparisons used to identify outliers: (a) temperature profiles for 28 April 1992, and (b) temperature profiles for the 5 February 1992, showing an outlier in the sensor #2 concrete temperature profile.

February, March and November were considered adequate while the size of the sample spaces associated with the remaining months (excluding December) were deemed more than sufficient for the validation purpose. It is assumed that the sample space for every month except January and December is sufficiently large such that any atypical or unusual feature of a diurnal temperature curve will be averaged out in the statistics, so as to not significantly affect the mean results for a particular month.

Figure 3-1(b) contains plots of the filtered data for the air and concrete daily temperature profiles for the month of April. In particular, note that the filtered data for the concrete temperature profiles are significantly cleaner than the original raw data (shown in Figure 3-1(a)). The filtered data for the air temperature case does not vary significantly from the raw data because the thermal sensor recording the air temperatures was not as prone to malfunctions as the thermal sensors measuring the concrete temperatures.

Having filtered the experimental data for outliers, the mean and standard deviation of the temperature profiles were computed for each month. The statistics of the air and the concrete temperature profiles for the month of April are shown in Figure 3-1(c). The error

| | - Air Temperature Profiles | | | Concrete Temperature Profiles | | |
|-----------|----------------------------|---------------|-------|-------------------------------|---------------|-------|
| | Data Sets | Rejected Sets | Total | Data Sets | Rejected Sets | Total |
| January | 2 | 1 | 1 | 4 | 2 | 2 |
| February | 22 | 4 | 18 | 44 | 12 | 32 |
| March | 67 | 4 | 63 | 134 | 54 | 80 |
| April | 90 | 3 | 87 | 180 | 41 | 139 |
| May | 93 | 3 | 90 | 186 | 40 | 146 |
| June | 90 | 4 | 86 | 180 | 38 | 142 |
| July | 93 | 2 | 91 | 186 | 35 | 151 |
| August | 93 | 1 | 92 | 186 | 33 | 153 |
| September | 86 | 4 | 82 | 172 | 34 | 138 |
| October | 61 | 3 | 59 | 122 | 9 | 113 |
| November | 39 | 3 | 36 | 78 | 27 | 51 |
| December | - | - | - | - | - | - |

Table 3-4: Summary of sample space sizes for each month listing the number of raw data sets, the number of data sets that were incomplete or contained outliers, and the final total sample space size.

bars in these plots represent the mean profile with an error of one standard deviation. Assuming an unbiased sample space and Gaussian statistics, 68.25 % of all temperatures (measured or predicted for this particular location) would be expected to lie within one standard deviation of the mean at any instant in time. A proportion of 95.46 % and 99.73 % should lie within two and three standard deviations of the mean, respectively. The plots of the statistics for the months from February to November can be found in Figure 3-5 and Figure 3-6.

3.3 Validation of Temperature Prediction Model

Complete 24-hour diurnal temperature profiles were computed using the MAT for the materials air and concrete for the specified longitudinal and latitudinal coordinates of the location in northern Australia being considered. Air temperatures were computed by stipulating a blackbody in the material specification with an altitude of 108 m. This altitude was chosen because the location in northern Australia has an elevation of 108 m above sea level. Results were obtained for every month of the year, and the standard heat transfer parameter files included with the SensorVision package were employed in the simulations.

Several MAT characteristics were noted during the validation process. In the case of the air temperature computations, the same MAT results were obtained regardless of the year specified. In addition, the temperatures were identical for the first day to the penultimate day of each month. Temperature predictions for the last day of each month matched the results for the next month, provided the specified month was February, April, June, July, or November. Temperature predictions for the last day of January, March, May, August, September and October were unique within the year. The MAT results for all days in December were identical. Figure 3-3 summarises the MAT characteristics described above by graphically illustrating the days of the year for which identical air temperature profiles are predicted. In the case of the concrete temperature profiles, results were unique for all days in the year. However, the variations from one day to the next were minor and incremental except between days that also experienced a change in the air temperature predictions. Differences in results were noted between years but these differences were considered negligible. The reasons for these peculiar patterns of predicted temperature profiles as a function of the day of year are unknown. Although these MAT characteristics have no perceivable affect on the validation effort, they were mentioned above as a matter of curiosity and for the sake of completeness. In the validation effort, the air and concrete surface temperatures were computed for every hour during the 15th day of each month for the year 1991. These results were considered representative of typical MAT predicted values for each month of the year. Other pertinent MAT input parameters used in the simulations include: the default

atmospheric model for the location and day of year; mean temperature, humidity, and wind; clear cloud cover with a cloud base altitude of 1 km; and a visibility range of 23 km.

Initially, the MAT predicted temperatures were compared against records obtained from the (Australian) Bureau of Meteorology. For the particular location in northern Australia, averaged 9 a.m. and 3 p.m. air temperatures for each month (collected over 14 and 13 years, respectively) were available. Figure 3-4 shows the comparisons between the MAT predicted air temperatures and the Bureau of Meteorology data. As evident in the plots, reasonable agreement is attained for the 9 a.m. air temperature results for all months, except September, October and November. The MAT consistently under-predicts the 3 p.m. air temperatures for this location.

The MAT generated diurnal temperature profiles and the experimental data (processed in Section 3.2) are plotted in Figure 3-5 and Figure 3-6. The air temperature diurnal profiles are shown in Figure 3-5 while Figure 3-6 contains the concrete diurnal temperature profiles. It is apparent from these plots that the MAT generated results do not compare well to the experimental data. With regard to the air temperature profiles, the predicted results have significantly smaller diurnal ranges than that exhibited by the measured data. There is a provision in the MAT program to include an extension in the MAT input file to calibrate the computed temperature profiles. In this extension, an air

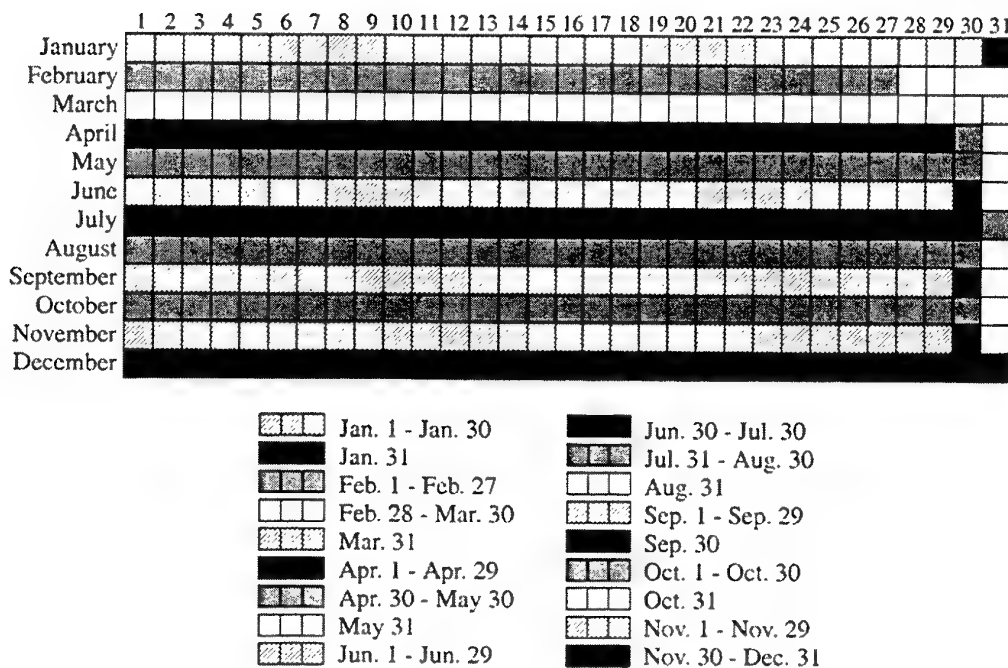


Figure 3-3: Diagram showing the days of the year for which the MAT predicts identical daily temperature profiles.

temperature and time of day are specified. The air temperature curves are then calibrated, such that the specified air temperature is obtained at the specified time. The net effect of the extension is to move the predicted temperature profiles up or down, but there is negligible effect on the diurnal range. Consequently, the MAT generated temperatures cannot be made to coincide with the empirical data to any acceptable level. This problem is attributed to differences between the standard atmospheric (tropical summer and tropical winter) models employed by the MOSART code and the actual atmospheric profile at the location under consideration. The MOSART code was predominantly developed for application to northern hemisphere regions, hence problems with its application to this southern hemisphere tropical zone was not entirely unexpected. Discussions with MultiGen-Paradigm have revealed that a modification in the MOSART code is planned in future upgrades of the MAT, which will allow users to define appropriate atmospheric profiles for a geo-specific location. This functionality is expected to appear in version 3.5 of SensorVision. Until user-specified atmospheric profiles are supported, it is concluded that the MAT cannot satisfactorily predict air temperatures for the geo-specific location in northern Australia being considered.

The predicted concrete temperature profiles also show poor agreement with the experimental data. Although the shape of the curves are similar, most of the predicted temperature data lie outside of the error bars plotted in Figure 3-6. However, unlike the air temperature case, the error in the MAT predicted concrete temperatures may be due

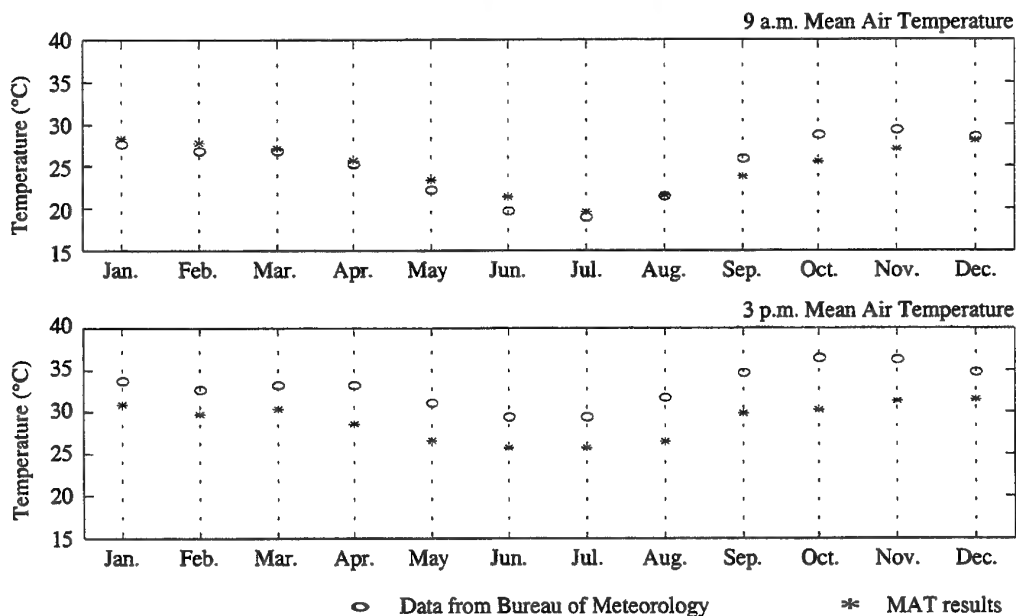


Figure 3-4: Comparisons of the MAT generated results with mean 9 a.m. and 3 p.m. air temperatures obtained from the (Australian) Bureau of Meteorology.

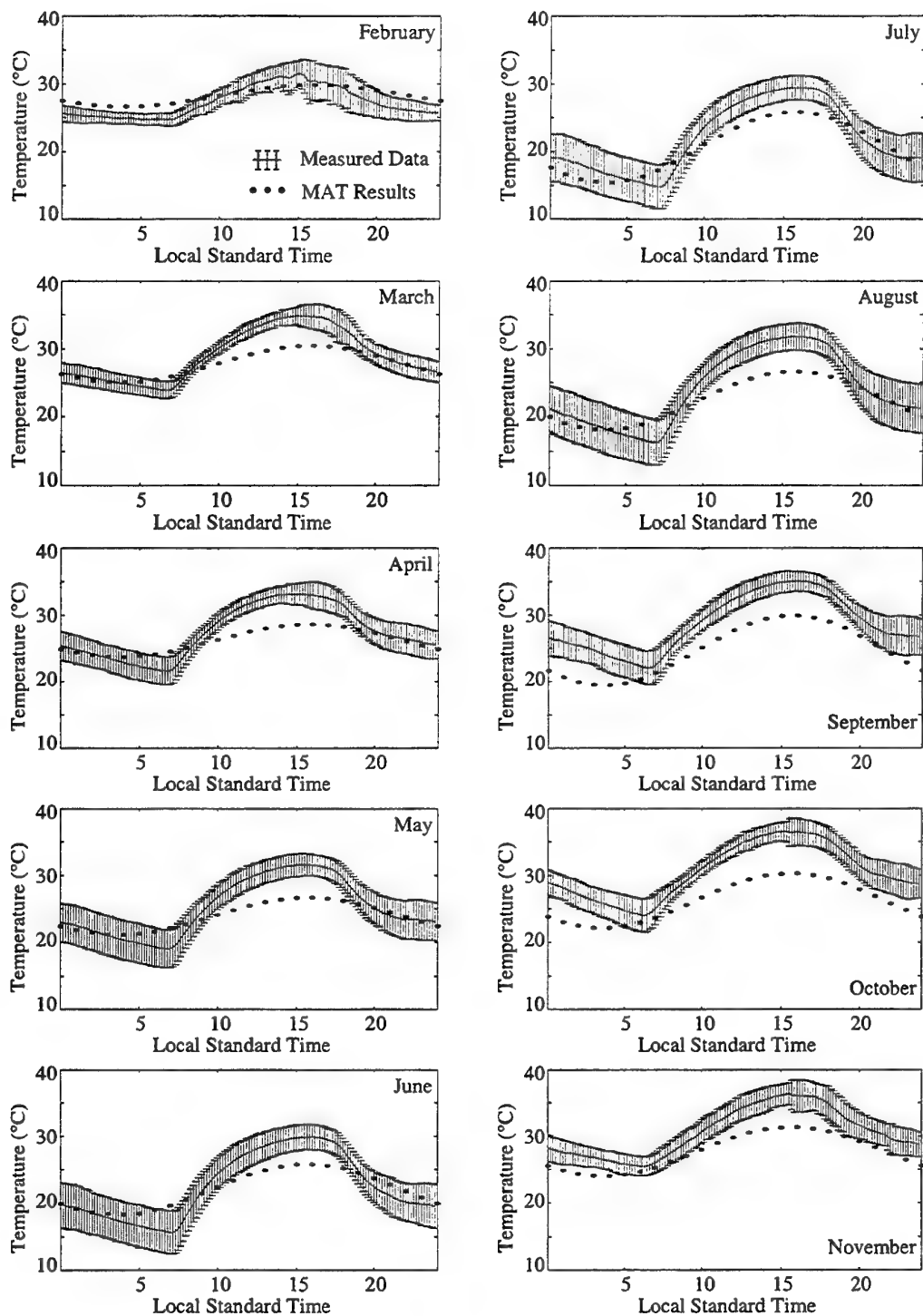


Figure 3-5: Comparison between the MAT generated and measured diurnal air temperature profiles for the months from February to November.

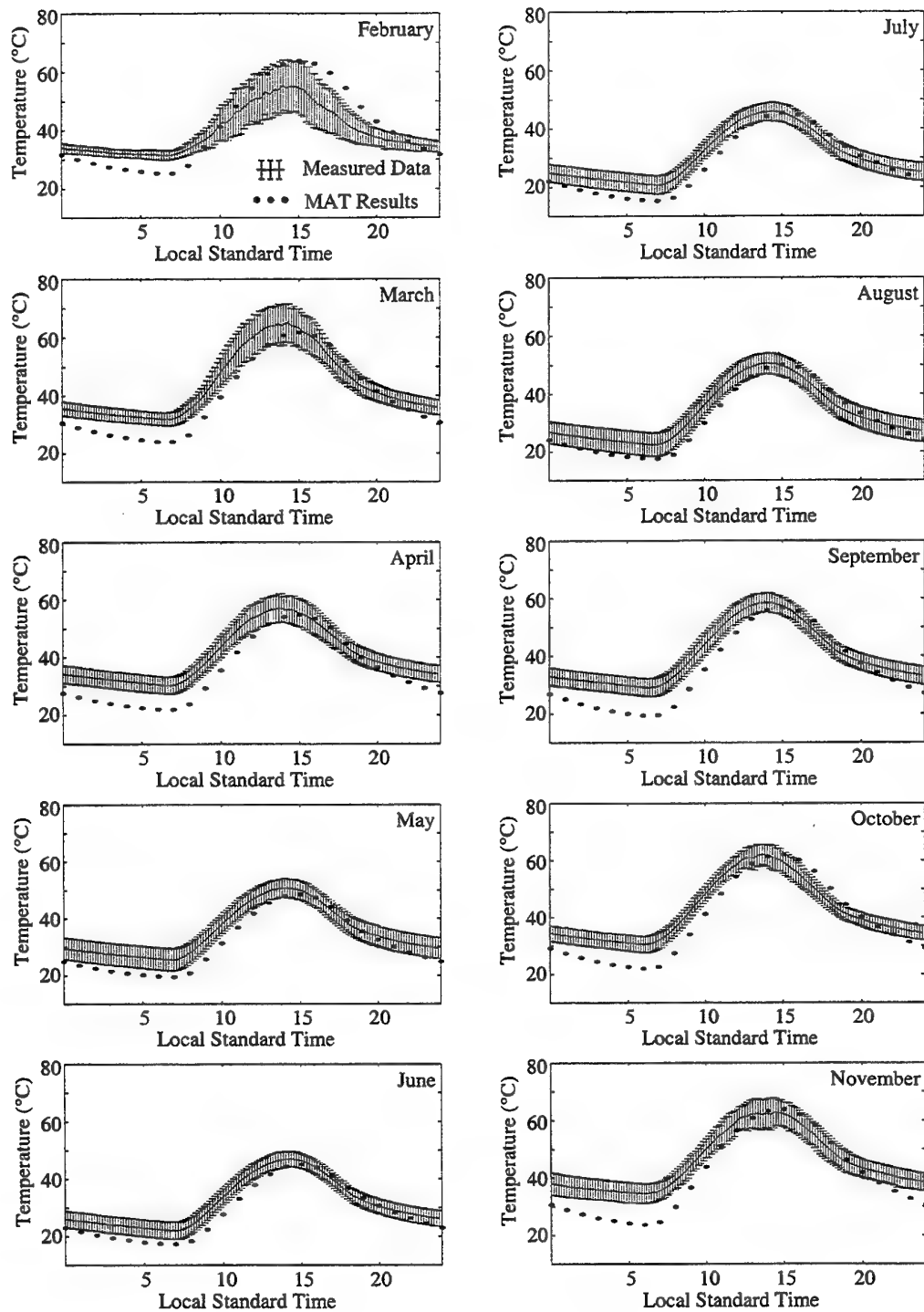


Figure 3-6: Comparison between the MAT generated and measured diurnal concrete temperature profiles for the months from February to November.

to incorrect heat transfer parameters for the actual concrete sample used in the trials. In a more rigorous validation effort, the heat transfer parameters for the concrete sample would be measured. Unfortunately, physical access to the concrete sample was not possible, hence a more heuristic approach of approximating the heat transfer parameters was adopted [5]. The heat transfer parameters were modified until a good match was achieved between the predicted concrete temperature profiles and the empirical data. The effects of individually varying solar absorptivity, thermal emissivity, specific heat, thermal conductivity, and material density on the concrete diurnal temperature profile computed for April are shown in the plots of Figure 3-7. Nearly all features of the temperature profile could be varied. The exception was the temperature minimum (occurring around 7 a.m.), which could not be made to coincide well with the empirical data while simultaneously maintaining a realistic thermal emissivity value. This

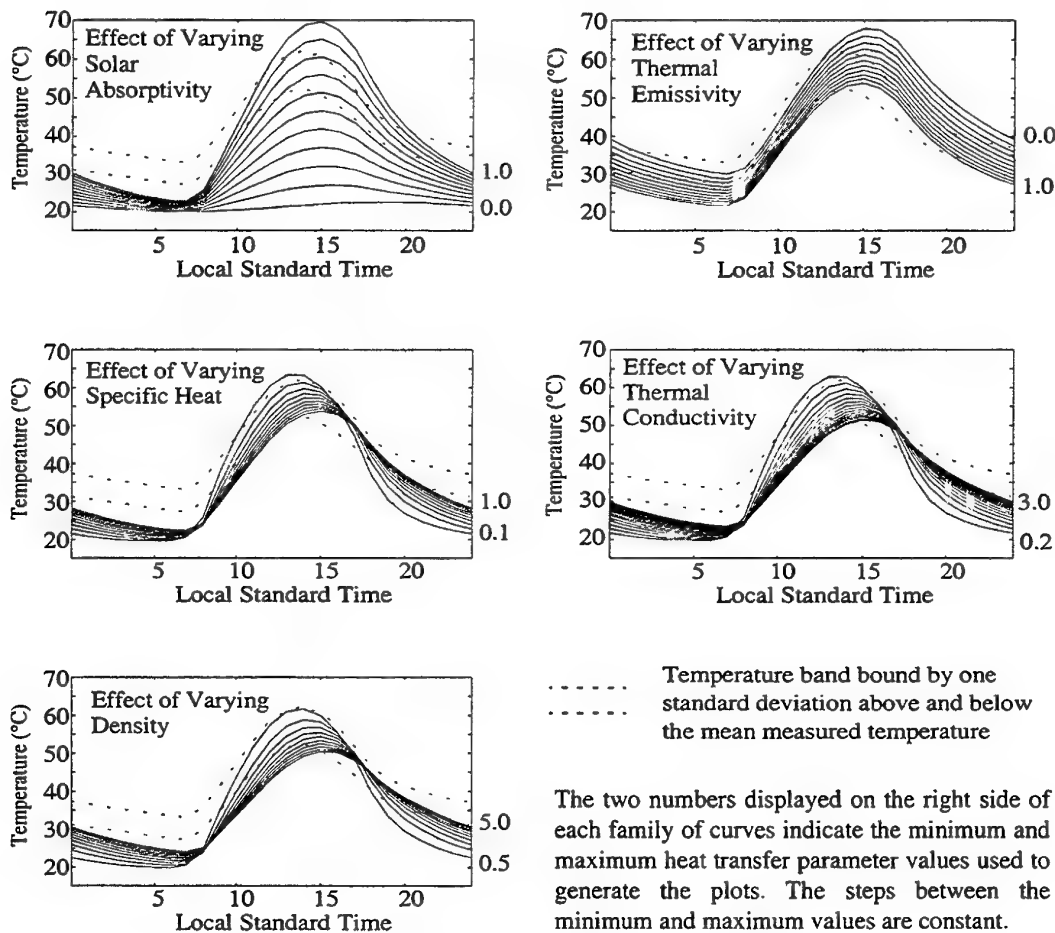


Figure 3-7: Graphs illustrating the effect of varying heat transfer parameters on the MAT predicted concrete diurnal temperature profiles for the month of April.

problem is most likely due to the MAT incorrectly predicting the air temperatures. A fix was obtained by exploiting the MAT extension (described above) to artificially move the temperature profiles up. The use of the MAT extension is only a superficial solution in the sense that it would be ineffective if more than one material was specified in the MAT input file. A proper solution to the problem requires modifications to be made to the MOSART program to ensure that air temperatures are accurately predicted for the geo-specific location considered.

Using essentially a trial-and-error process, a combination of heat transfer parameters that resulted in a good general agreement between the MAT generated concrete temperature profiles and the measured data was obtained. The modified heat transfer parameter values are listed in Table 3-5. Note that these values are sensible and realistic. The significant change in value of thermal conductivity of concrete from $1.73 \text{ W m}^{-1} \text{ K}^{-1}$ to $0.5 \text{ W m}^{-1} \text{ K}^{-1}$ is reasonable, given that a figure of $0.84 \text{ W m}^{-1} \text{ K}^{-1}$ was quoted in a textbook [6]. The final concrete temperature profiles are plotted in Figure 3-8. Note that the values of the 7 a.m. temperatures defined in the MAT extensions were varied for each month to counter the problem of incorrectly predicted air temperatures. Furthermore, the values employed were unrealistic (ranging from 27°C to 42°C) due to the fact that the MAT generated air temperatures had an erroneous diurnal range compared with the empirical data. The 7 a.m. value used in the MAT extension for each month is indicated in the top

| Heat Transfer Parameter | Original | Modified |
|-------------------------|---|--|
| Label | Concrete | Concrete |
| Default Material | Concrete | Concrete |
| Solar Absorptivity | 0.6681411 | 0.4 |
| Thermal Emissivity | 0.9333010 | 0.9 |
| Characteristic Length | 1.00 m | 1.00 m |
| Evaporation Index | No | No |
| Specific Heat | $0.88 \text{ J gm}^{-1} \text{ K}^{-1}$ | $0.7 \text{ J gm}^{-1} \text{ K}^{-1}$ |
| Thermal Conductivity | $1.73 \text{ W m}^{-1} \text{ K}^{-1}$ | $0.5 \text{ W m}^{-1} \text{ K}^{-1}$ |
| Density | $2.4 \times 10^{-6} \text{ gm m}^{-3}$ | $2.3 \times 10^{-6} \text{ gm m}^{-3}$ |
| Surface Layer Thickness | 0.35 m | 0.35 |
| Sub-layer 1 Thickness | 0.15 m | 0.15 |
| Sub-layer 1 Material | Road Gravel | Road Gravel |
| Sub-layer 2 Material | Packed Dirt | Packed Dirt |

Table 3-5: List of original and modified heat transfer parameters.

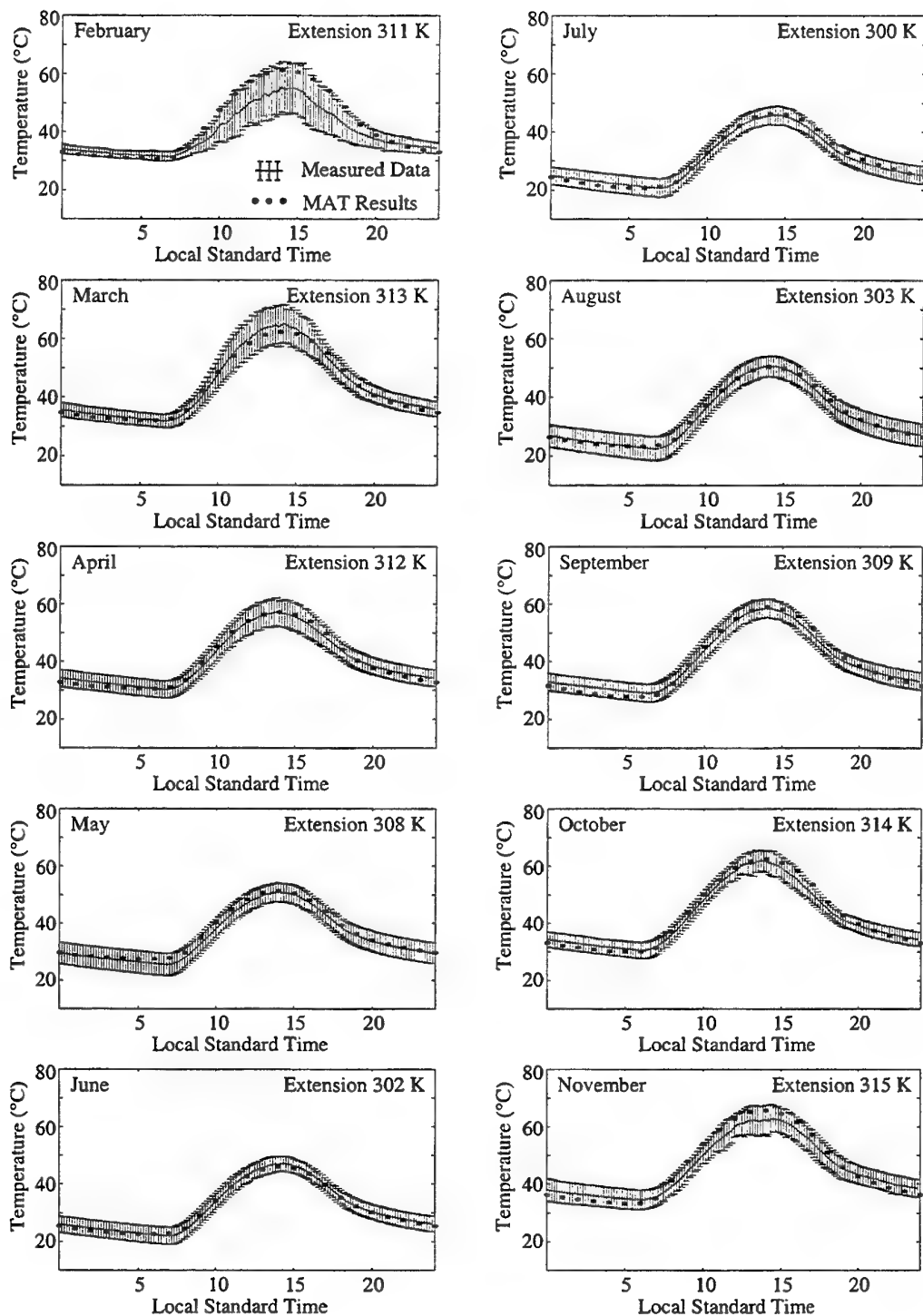


Figure 3-8: Comparison between the MAT results with modified concrete heat transfer parameters and measured diurnal concrete temperature profiles.

right corner of the relevant plots in Figure 3-8. The overall agreement of the MAT predicted concrete temperatures using the modified heat transfer parameters with the measured data is extremely good for most months. The poorest agreement was obtained in February, and these results are still considered reasonable. Recall that the size of the sample space of the measured data in February was only considered adequate, hence a high level of confidence is not associated with the statistics corresponding to this month.

The variation of material heat transfer parameters to obtain an acceptable match between measured and predicted temperature data is a feasible technique for generating validated material temperature profiles. However, the method can only be employed once the problem with the air temperature predictions has been fixed.

3.4 Chapter Summary

Results of an experimental validation of the SensorVision temperature prediction model were presented in this chapter. SensorVision generated diurnal air and concrete temperature profiles were compared against experimental data obtained from a location in northern Australia. It was observed that the SensorVision results did not compare well with the empirical data. In particular, the predicted diurnal air temperature ranges were significantly smaller than those measured. These inaccuracies were attributed to differences between the actual atmospheric profile at the geo-specific location and the standard atmospheric models employed by the MOSART code. This problem should be resolved in future software upgrades of SensorVision, which are expected to include functionality for users to custom define atmospheric profiles. Until user-defined atmospheric profiles are supported in the MAT, the physical accuracy of the temperature models employed by SensorVision cannot be properly evaluated.

Predicted concrete temperature profiles compared well with the empirical data after modifications were made to the concrete heat transfer parameters. However, it was necessary to use a MAT extension to artificially inflate air temperatures in order to achieve good agreement between predicted and measured results. The use of the MAT extension is only a superficial solution in the sense that the air temperature values employed were unrealistic, and the use of the extension would be ineffective if more than one material was specified in the MAT input file. A proper solution to the problem requires modifications to be made to the MOSART program to ensure that air temperatures are accurately predicted for the geo-specific location considered.

4. Conclusions and Further Work

This report presented the results from a validation conducted on the SensorVision thermal emission model. The thermal emission model essential involves two components: the prediction of an object's surface temperature given the surrounding conditions; and the calculation of the radiance incident on a sensor due to that object as a result of thermal emission processes. The validation effort described in this report considered the temperature prediction model as well as the radiance computation model.

The SensorVision radiance computation model was validated mathematically against an accurate non-real time thermal emission model. SensorVision employs an approximation whereby spectral terms within the thermal emission equation are moved outside of the spectral integration and replaced by their in-band averaged values. This approximation is required to enable real-time operation. The effect of the approximation on the accuracy of the SensorVision thermal emission model was analysed and a figure of merit was developed to enable quick determination of likely error levels. The figure of merit was based on the second moment of the spectral variables and was referred to as the error indicator or EI. The main purpose of the EI is to aid users during simulation construction to identify scenario components that may impact on the integrity of the HIL simulation. The main conclusion that can be drawn from the validation of the radiance computation model is that SensorVision appears to be more suited to LWIR simulations than MWIR simulations. The reasons for this conclusion are three-fold:

- the variability of the spectral emissivities of materials tend to be lower in the LWIR band compared to the MWIR band;
- the spectral atmospheric transmission coefficient does not vary much in the LWIR band compared to the MWIR band; and
- simulations tend to involve objects with temperatures near ambient temperature, which results in smaller error levels in the LWIR band and higher error levels in the MWIR band.

Given that IR phenomenology in the LWIR band is emission dominated, it can be concluded that SensorVision can be confidently employed in HIL simulations involving LWIR seekers (provided the prediction or assignment of surface temperatures is accurate). HIL simulations involving MWIR seekers, using SensorVision, should be constructed with care. The validation has shown that significant errors can be generated by the SensorVision thermal emission model in the MWIR band. These errors can be mitigated by carefully choosing the materials and engagement geometries employed in the simulation scenarios. Furthermore, simulations associated with narrower bands than the full 3 to 5 μm band tested during the validation are likely to yield lower levels of error. Confidence in the use of SensorVision for MWIR HIL simulations requires the

validation of reflection components of the IR radiometric equation, since reflection phenomena are significant in the MWIR band.

SensorVision employs a standard atmospheric program called the MOSART code to predict surface temperatures of objects prior to the real-time simulation. The temperature prediction model was validated against experimental data obtained from trials conducted in northern Australia. During these trials, daily temperature profiles were measured for air and a concrete sample. In the validation, the MOSART predicted temperatures were compared against empirical data and it was shown that the temperature prediction model was not accurate for the particular location in northern Australia. The reason for the poor agreement between the predicted and empirical data was attributed to differences between the tropical atmospheric model used by the MOSART code and the atmospheric profile at the location in northern Australia. The inability of SensorVision to allow users to specify custom atmospheric profiles was considered a significant problem in the current software. Fortunately, the next release of SensorVision is expected to provide the functionality for user defined atmospheric profiles. The results for the concrete temperature profile comparisons showed the importance of providing correct material heat transfer parameters. Heat transfer parameters can be derived heuristically by matching the SensorVision generated temperature profiles with the empirical data.

Further work is required to complete the verification and validation of SensorVision. In particular, the following tasks still need to be performed.

- The reflection components of the IR radiometric equation need to be validated to determine its effect on MWIR simulations.
- Verification of the SensorVision algorithm is still required. The accuracy associated with the use of lookup tables and the exactitude of employing extrapolation techniques to approximate various parameters should be investigated.
- The effects of digital artifacts on HIL simulations should be explored [1]. The effects of alias induced scintillations, pixel bit resolution, and z-buffer fighting have the potential to compromise the integrity of HIL simulation results.
- Finally, procedures for the validation of particular SensorVision simulations should be proposed. In particular, accurate and realistic non-real-time models should be developed or acquired for the purposes of cross-validation in post-processing HIL simulation activities.

5. References

- [1] N. Duong, and M. Wegener, *SensorVision Radiometric Equations Version 2.2*, DSTO Technical Report, DSTO-TN-0193, Melbourne: DSTO AMRL, Feb. 1999.
- [2] S. T. Caplan, *Verification and Validation of SensorVision - Summary of Papers and Proposal for Validation Work*, DERA report, Aug. 1988.
- [3] N. Duong, and M. Wegener, "SensorVision Validation: Diurnal Temperature Variations in Northern Australia", *Proc. SPIE - Technologies for Synthetic Environments: Hardware-In-The-Loop Testing V*, Orlando, Florida, 24 - 28 Apr. 2000.
- [4] D. C. Anding, *SensorVision Technical Description*, Paradigm Simulation Inc., San Diego, 28 Apr. 1998.
- [5] D. C. Anding, *Special Technical Report: Validation of SensorVision*, Paradigm Simulation Inc., San Diego, 1 Jun. 1998.
- [6] D. C. Giancoli, *Physics for Scientists and Engineers with Modern Physics*, 2nd Ed., New Jersey: Prentice-Hall, 1988.

Appendix A: Using Error Indicators

The purpose of error indicators is to help users determine the likely level of errors associated with using SensorVision in the generation of IR simulations. All error indicators have a possible range of zero to 100, where a value of 100 represents the worst case. There are error indicators associated with the spectral emissivity of materials, the spectral atmospheric transmission coefficient, and the Planck's blackbody spectral radiance parameter. Furthermore, the error indicators can be combined to give the collective effect of spectral variations in the material emissivity, the atmospheric transmission coefficient, and the Planck's blackbody curve on the SensorVision generated errors. This appendix provides the equations and data required to use error indicators for a range of possible situations. The wavebands considered include the MWIR band (nominally specified as the band from 3 to 5 μm) and the LWIR band (nominally specified as the band from 8 to 12 μm).

A.1 Error Indicators for Material Emissivities

The EI values for the spectral emissivities of materials can be calculated using

$$EI_{\epsilon} = 200e_{\epsilon}, \quad (\text{A-1})$$

where e_{ϵ} is the second moment of the spectral emissivity data. The second moments for a range of materials are listed in Table A-1, Table A-2, Table A-3, Table A-4, and Table A-5.

| Composite Materials | 3 - 5 μm band | | 8 - 12 μm band | |
|---------------------|--------------------------|----------------|---------------------------|----------------|
| | $\bar{\epsilon}$ | e_{ϵ} | $\bar{\epsilon}$ | e_{ϵ} |
| beige_fabric | 0.3789 | 0.0297 | 0.2705 | 0.0249 |
| black_rubber | 0.0428 | 0.0013 | 0.0468 | 0.0036 |
| brown_plastic | 0.1085 | 0.0419 | 0.0526 | 0.0101 |
| cream_fiberglass | 0.0468 | 0.0010 | 0.0467 | 0.0060 |
| gold_nylon | 0.1647 | 0.0863 | 0.0861 | 0.0327 |
| green_canvas | 0.0675 | 0.0255 | 0.0379 | 0.0133 |
| grey_fabric | 0.3926 | 0.0276 | 0.3513 | 0.0470 |
| olive_plastic | 0.1378 | 0.0453 | 0.0251 | 0.0014 |
| orange_epoxy | 0.0363 | 0.0010 | 0.0385 | 0.0023 |
| red_nylon | 0.0460 | 0.0055 | 0.0440 | 0.0040 |
| tan_felt | 0.1743 | 0.0945 | 0.0580 | 0.0242 |
| white_fabric | 0.2279 | 0.0446 | 0.0241 | 0.0035 |
| yellow_silicon | 0.1578 | 0.0761 | 0.0751 | 0.0337 |
| asphalt_shingles | 0.0684 | 0.0198 | 0.0540 | 0.0210 |

Table A-1: Emissivity mean and second moment values for different composite materials.

| Construction Materials | 3 - 5 μm band | | 8 - 12 μm band | |
|------------------------|--------------------------|----------------|---------------------------|----------------|
| | $\bar{\epsilon}$ | e_{ϵ} | $\bar{\epsilon}$ | e_{ϵ} |
| black_asphalt | 0.0516 | 0.0097 | 0.0531 | 0.0136 |
| block_concrete | 0.1064 | 0.0306 | 0.0573 | 0.0169 |
| clear_glass | 0.0305 | 0.0080 | 0.1888 | 0.1231 |
| dark_titanium | 0.6908 | 0.0197 | 0.7889 | 0.0098 |
| metal_roof | 0.7930 | 0.0298 | 0.8731 | 0.0068 |
| oxydized_aluminum | 0.7631 | 0.0674 | 0.8065 | 0.0193 |
| paved_concrete | 0.0561 | 0.0183 | 0.0334 | 0.0107 |
| pebbled_asphalt | 0.0684 | 0.0198 | 0.0540 | 0.0210 |
| pine_wood | 0.1220 | 0.0509 | 0.0537 | 0.0181 |
| red_brick | 0.2739 | 0.0870 | 0.0424 | 0.0226 |
| roof_tar | 0.0488 | 0.0016 | 0.0418 | 0.0016 |
| rusting_steel | 0.6963 | 0.0330 | 0.8206 | 0.0120 |
| urban_commercial | 0.0491 | 0.0170 | 0.0273 | 0.0041 |
| urban_residential | 0.1209 | 0.0582 | 0.0689 | 0.0038 |
| wood_siding | 0.1012 | 0.0344 | 0.0438 | 0.0083 |

Table A-2: Emissivity mean and second moment values for different construction materials.

| Paints | 3 - 5 μm band | | 8 - 12 μm band | |
|-----------------|--------------------------|----------------|---------------------------|----------------|
| | $\bar{\epsilon}$ | e_{ϵ} | $\bar{\epsilon}$ | e_{ϵ} |
| ash_grey | 0.0667 | 0.0064 | 0.0483 | 0.0093 |
| battleship_grey | 0.0241 | 0.0012 | 0.0346 | 0.0082 |
| blackish_brown | 0.1589 | 0.0405 | 0.0636 | 0.0181 |
| bleached_yellow | 0.0792 | 0.0199 | 0.0231 | 0.0049 |
| canary_yellow | 0.0814 | 0.0214 | 0.0541 | 0.0098 |
| dark_tan | 0.1088 | 0.0329 | 0.0560 | 0.0162 |
| jet_black | 0.0412 | 0.0013 | 0.0531 | 0.0064 |
| kelly_green | 0.0457 | 0.0022 | 0.0471 | 0.0070 |
| light_red | 0.0708 | 0.0223 | 0.0291 | 0.0086 |
| light_tan | 0.0852 | 0.0101 | 0.0548 | 0.0135 |
| mint_green | 0.0450 | 0.0114 | 0.0208 | 0.0066 |
| mustard_yellow | 0.3008 | 0.0871 | 0.1271 | 0.0164 |
| off_white | 0.1076 | 0.0484 | 0.0447 | 0.0092 |
| olive_green | 0.0926 | 0.0223 | 0.0537 | 0.0122 |
| sky_blue | 0.0918 | 0.0211 | 0.0321 | 0.0091 |
| snow_white | 0.2060 | 0.0992 | 0.0540 | 0.0183 |

Table A-3: Emissivity mean and second moment values for different types of paints.

| Soils | 3 - 5 μm band | | 8 - 12 μm band | |
|---------------------|--------------------------|----------------|---------------------------|----------------|
| | $\bar{\epsilon}$ | e_{ϵ} | $\bar{\epsilon}$ | e_{ϵ} |
| beach_sand | 0.3075 | 0.1456 | 0.0650 | 0.0334 |
| black_sand | 0.0886 | 0.0176 | 0.0779 | 0.0445 |
| clay_soil | 0.2835 | 0.0808 | 0.0761 | 0.0402 |
| compact_soil | 0.1034 | 0.0319 | 0.0409 | 0.0070 |
| desert_sand | 0.1677 | 0.0692 | 0.0610 | 0.0215 |
| dry_lakebed | 0.3115 | 0.0929 | 0.0650 | 0.0334 |
| dry_seabed | 0.3609 | 0.1058 | 0.0634 | 0.0318 |
| fresh_snow | 0.0170 | 0.0052 | 0.0080 | 0.0038 |
| ice | 0.0225 | 0.0121 | 0.0163 | 0.0089 |
| lake_sand | 0.1379 | 0.0649 | 0.0916 | 0.0470 |
| limestone-silt | 0.1631 | 0.0245 | 0.0834 | 0.0248 |
| limestone-silt-sand | 0.1269 | 0.0125 | 0.0515 | 0.0084 |
| limestone-silt-soil | 0.1808 | 0.0388 | 0.0756 | 0.0147 |
| limestone_rock | 0.1459 | 0.0293 | 0.0924 | 0.0367 |
| loam_soil | 0.1110 | 0.0425 | 0.0286 | 0.0049 |
| loamy_sand | 0.1763 | 0.0866 | 0.1221 | 0.0846 |
| lump_coal | 0.0269 | 0.0028 | 0.0212 | 0.0026 |
| old_snow | 0.0152 | 0.0050 | 0.0093 | 0.0034 |
| road_gravel | 0.1191 | 0.0511 | 0.0496 | 0.0157 |
| salt-silt | 0.1720 | 0.0352 | 0.1016 | 0.0022 |
| sand-soil | 0.1649 | 0.0379 | 0.0483 | 0.0134 |
| sandstone-soil | 0.1163 | 0.0226 | 0.0565 | 0.0152 |
| sandstone_rock | 0.1459 | 0.0293 | 0.0924 | 0.0367 |
| sandy_loam | 0.1793 | 0.0635 | 0.0557 | 0.0303 |
| scrub-soil | 0.1808 | 0.0388 | 0.0756 | 0.0147 |
| scrub-soil (shaded) | 0.1507 | 0.0562 | 0.0216 | 0.0024 |
| silt-sand | 0.2700 | 0.0863 | 0.0433 | 0.0159 |
| silty_clay | 0.0725 | 0.0224 | 0.0286 | 0.0047 |
| silty_loam | 0.3609 | 0.1058 | 0.0634 | 0.0318 |
| tilled_soil | 0.2982 | 0.1248 | 0.0678 | 0.0193 |
| varnished_sand | 0.0176 | 0.0050 | 0.0106 | 0.0020 |
| varnished_sandstone | 0.1255 | 0.0163 | 0.0650 | 0.0334 |
| water | 0.1255 | 0.0163 | 0.0650 | 0.0334 |
| wet_lakebed | 0.0607 | 0.0180 | 0.0259 | 0.0032 |
| wet_seabed | 0.0389 | 0.0279 | 0.0623 | 0.0727 |
| wet_soil | 0.0696 | 0.0114 | 0.0185 | 0.0010 |
| white_sand | 0.0668 | 0.0084 | 0.0499 | 0.0010 |

Table A-4: Emissivity mean and second moment values for different types of soils.

| Vegetation | 3 - 5 μm band | | 8 - 12 μm band | |
|---------------------------|--------------------------|----------------|---------------------------|----------------|
| | $\bar{\epsilon}$ | e_{ϵ} | $\bar{\epsilon}$ | e_{ϵ} |
| broadleaf | 0.0767 | 0.0197 | 0.0419 | 0.0060 |
| broadleaf (shaded) | 0.0804 | 0.0180 | 0.0726 | 0.0059 |
| broadleaf-pine | 0.0405 | 0.0032 | 0.0395 | 0.0031 |
| broadleaf-pine (shaded) | 0.0380 | 0 | 0.0702 | 0.0030 |
| broadleaf-scrub | 0.1880 | 0.0729 | 0.1072 | 0.0410 |
| broadleaf-scrub (shaded) | 0.1762 | 0.0649 | 0.1358 | 0.0397 |
| dry_grass | 0.1447 | 0.0534 | 0.0756 | 0.0240 |
| dry_grass (shaded) | 0.1426 | 0.0474 | 0.1052 | 0.0232 |
| grass-scrub | 0.1373 | 0.0469 | 0.0674 | 0.0149 |
| grass-scrub (shaded) | 0.1249 | 0.0415 | 0.0973 | 0.0144 |
| grass-soil | 0.0385 | 0.0026 | 0.0371 | 0.0024 |
| grass-soil (shaded) | 0.0370 | 0.0015 | 0.0679 | 0.0023 |
| lawn_grass | 0.0534 | 0.0061 | 0.0310 | 0.0021 |
| lawn_grass (shaded) | 0.0509 | 0.0036 | 0.0620 | 0.0020 |
| pine | 0.0918 | 0.0110 | 0.0270 | 0.0041 |
| pine (shaded) | 0.0943 | 0.0098 | 0.0581 | 0.0040 |
| pine-broadleaf | 0.0825 | 0.0152 | 0.0100 | 0 |
| pine-broadleaf (shaded) | 0.0747 | 0.0077 | 0.0417 | 0 |
| pine-scrub | 0.1282 | 0.0436 | 0.0617 | 0.0131 |
| pine-scrub (shaded) | 0.1218 | 0.0388 | 0.0918 | 0.0127 |
| scrub | 0.1025 | 0.0316 | 0.0421 | 0.0017 |
| scrub (shaded) | 0.0980 | 0.0275 | 0.0727 | 0.0017 |
| scrub-grass-soil | 0.1012 | 0.0344 | 0.0438 | 0.0083 |
| scrub-grass-soil (shaded) | 0.1089 | 0.0299 | 0.0744 | 0.0081 |
| tree_bark | 0.1012 | 0.0344 | 0.0438 | 0.0083 |
| tree_bark (shaded) | 0.1089 | 0.0299 | 0.0744 | 0.0081 |
| tundra | 0.0967 | 0.0198 | 0.0527 | 0.0040 |
| tundra (shaded) | 0.0940 | 0.0225 | 0.0830 | 0.0039 |

Table A-5: Emissivity mean and second moment values for different types of vegetation.

A.2 Error Indicators for the Atmospheric Transmission Coefficient

The EI values for spectral atmospheric transmission coefficients can be calculated using

$$EI_{\tau} = 200e_{\tau}, \quad (\text{A-2})$$

where e_{τ} is the second moment of the spectral atmospheric transmission coefficient data. The second moments for a range of LOS (line of sight) paths are listed in Table A-6.

| Path Description | Range | 3 - 5 μm band | | 8 - 12 μm band | |
|--------------------------|-------|--------------------------|------------|---------------------------|------------|
| | | $\bar{\tau}$ | e_{τ} | $\bar{\tau}$ | e_{τ} |
| Horizontal Path | 1 km | 0.5242 | 0.3618 | 0.6444 | 0.1381 |
| | 2 km | 0.4179 | 0.3466 | 0.4458 | 0.1399 |
| | 5 km | 0.2712 | 0.2881 | 0.1650 | 0.0943 |
| | 10 km | 0.1662 | 0.2112 | 0.0384 | 0.0350 |
| | 20 km | 0.0786 | 0.1198 | 0.0029 | 0.0041 |
| | 50 km | 0.0134 | 0.0265 | 0.0000 | 0.0000 |
| Slant Path 10° Elevation | 1 km | 0.5290 | 0.3618 | 0.6572 | 0.1374 |
| | 2 km | 0.4283 | 0.3483 | 0.4784 | 0.1411 |
| | 5 km | 0.2951 | 0.2986 | 0.2316 | 0.1108 |
| | 10 km | 0.2107 | 0.2457 | 0.1076 | 0.0716 |
| | 20 km | 0.1616 | 0.2081 | 0.0639 | 0.0505 |
| | 50 km | 0.1298 | 0.1803 | 0.0520 | 0.0436 |
| Slant Path 20° Elevation | 1 km | 0.5336 | 0.3618 | 0.6689 | 0.1366 |
| | 2 km | 0.4378 | 0.3496 | 0.5062 | 0.1416 |
| | 5 km | 0.3196 | 0.3103 | 0.2932 | 0.1227 |
| | 10 km | 0.2635 | 0.2820 | 0.2157 | 0.1069 |
| | 20 km | 0.2323 | 0.2614 | 0.1952 | 0.0999 |
| | 50 km | 0.2147 | 0.2480 | 0.1823 | 0.0963 |
| Slant Path 30° Elevation | 1 km | 0.5378 | 0.3617 | 0.6792 | 0.1359 |
| | 2 km | 0.4464 | 0.3508 | 0.5294 | 0.1416 |
| | 5 km | 0.3447 | 0.3216 | 0.3554 | 0.1319 |
| | 10 km | 0.3046 | 0.3029 | 0.3175 | 0.1258 |
| | 20 km | 0.2819 | 0.2891 | 0.3026 | 0.1216 |
| | 50 km | 0.2711 | 0.2823 | 0.2766 | 0.1234 |
| Slant Path 60° Elevation | 1 km | 0.5471 | 0.3614 | 0.6995 | 0.1339 |
| | 2 km | 0.4667 | 0.3544 | 0.5785 | 0.1417 |
| | 5 km | 0.3996 | 0.3394 | 0.4964 | 0.1422 |
| | 10 km | 0.3742 | 0.3292 | 0.4793 | 0.1400 |
| | 20 km | 0.3638 | 0.3235 | 0.4687 | 0.1388 |
| | 50 km | 0.3587 | 0.3215 | 0.4382 | 0.1463 |
| Slant Path 90° Elevation | 1 km | 0.5505 | 0.3613 | 0.7067 | 0.1332 |
| | 2 km | 0.4739 | 0.3557 | 0.5946 | 0.1415 |
| | 5 km | 0.4157 | 0.3434 | 0.5343 | 0.1429 |
| | 10 km | 0.3942 | 0.3351 | 0.5205 | 0.1412 |
| | 20 km | 0.3861 | 0.3310 | 0.5057 | 0.1416 |
| | 50 km | 0.3821 | 0.3295 | 0.4814 | 0.1492 |

Table A-6: Second moment and mean values for transmission coefficients of some LOS paths.

A.3 Error Indicators for Planck's Blackbody Spectral Radiance

The EI value for Planck's blackbody spectral radiance is defined as

$$EI_{bb} = 200e_{bb}, \quad (\text{A-3})$$

where e_{bb} is the second moment of the normalised Planck's blackbody spectral radiance. The blackbody spectral radiance is normalised by its peak value in the wave band of interest. The second moment of the normalised Planck's blackbody curve as a function of temperature is listed in Table A-7.

| Temperature | 3 - 5 μm band e_{bb} | 8 - 12 μm band e_{bb} |
|-------------|--------------------------------------|---------------------------------------|
| 200 | 0.2714 | 0.1854 |
| 225 | 0.2806 | 0.1409 |
| 250 | 0.2871 | 0.0943 |
| 275 | 0.2910 | 0.0490 |
| 300 | 0.2924 | 0.0291 |
| 325 | 0.2912 | 0.0531 |
| 350 | 0.2875 | 0.0799 |
| 375 | 0.2814 | 0.1006 |
| 400 | 0.2730 | 0.1168 |
| 425 | 0.2626 | 0.1297 |
| 450 | 0.2502 | 0.1402 |
| 475 | 0.2360 | 0.1488 |
| 500 | 0.2203 | 0.1560 |
| 525 | 0.2032 | 0.1620 |
| 550 | 0.1849 | 0.1671 |
| 575 | 0.1656 | 0.1715 |
| 600 | 0.1453 | 0.1753 |
| 625 | 0.1237 | 0.1786 |
| 650 | 0.1020 | 0.1816 |
| 675 | 0.0811 | 0.1842 |
| 700 | 0.0628 | 0.1864 |
| 725 | 0.0493 | 0.1885 |
| 750 | 0.0441 | 0.1903 |
| 775 | 0.0483 | 0.1920 |
| 800 | 0.0583 | 0.1935 |
| 825 | 0.0706 | 0.1949 |
| 850 | 0.0832 | 0.1962 |
| 875 | 0.0952 | 0.1973 |
| 900 | 0.1061 | 0.1984 |
| 925 | 0.1159 | 0.1994 |
| 950 | 0.1246 | 0.2003 |
| 975 | 0.1320 | 0.2011 |
| 1000 | 0.1387 | 0.2019 |

Table A-7: Second moment values for the normalised Planck's blackbody spectral radiance.

A.4 Combining Error Indicator Values

The error indicator associated with the product of the material emissivity and atmospheric transmission coefficient is given by

$$EI_{\varepsilon\tau} = 100 \times 2e_{\varepsilon\tau}, \text{ where} \quad (\text{A-4})$$

$$e_{\varepsilon\tau} = \bar{\varepsilon}\bar{\tau} \sqrt{\left(\frac{e_{\varepsilon}}{\bar{\varepsilon}}\right)^2 + \left(\frac{e_{\tau}}{\bar{\tau}}\right)^2}. \quad (\text{A-5})$$

Parameters $\bar{\varepsilon}$ and $\bar{\tau}$ are the mean emissivity and transmission coefficient, respectively, in the waveband of interest.

The total error indicator including the effect of Planck's blackbody spectral radiance is calculated using

$$EI_{total} = \frac{EI_{\varepsilon\tau}}{100} \times EI_{bb}. \quad (\text{A-6})$$

A.5 Equations for Calculating the Second Moment

The second moment of a variable is given by

$$e = \sqrt{\frac{\int_{\lambda_1}^{\lambda_2} (x_{\lambda} - \bar{x})^2 d\lambda}{(\lambda_2 - \lambda_1)}}, \text{ or} \quad (\text{A-7})$$

$$e = \sqrt{\frac{1}{N} \sum_{n=1}^N [x_{\lambda}(n) - \bar{x}]^2}. \quad (\text{A-8})$$

Equation (A-7) is applicable to a continuous variable x_{λ} with mean value \bar{x} , while (A-8) is applicable to a discrete variable $x_{\lambda}(n)$ of N samples.

DISTRIBUTION LIST

Validation of SensorVision Thermal Emission Model

Ninh Duong and Michael Wegener

AUSTRALIA

DEFENCE ORGANISATION

Task Sponsor

DASD

S&T Program

| | |
|---|---------------|
| Chief Defence Scientist | } shared copy |
| FAS Science Policy | |
| AS Science Corporate Management | |
| Director General Science Policy Development | |
| Counsellor Defence Science, London (Doc Data Sheet) | |
| Counsellor Defence Science, Washington (Doc Data Sheet) | |
| Scientific Adviser to MRDC Thailand (Doc Data Sheet) | |
| Scientific Adviser Policy and Command | |
| Navy Scientific Adviser (Doc Data Sheet and distribution list only) | |
| Scientific Adviser - Army (Doc Data Sheet and distribution list only) | |
| Air Force Scientific Adviser | |
| Director Trials | |

Aeronautical and Maritime Research Laboratory

Director
Chief of Weapons Systems Division
Research Leader Maritime Weapons Systems, WSD
Research Leader Air Weapons Systems, WSD
Research Leader Land Weapons Systems, WSD
Research Leader Joint and Intelligence, WSD
Head Missile Simulation Group, WSD
Head Electro-Optical Seekers, WSD
Head Advance Concepts, WSD
Head Weapons Systems Analysis, WSD
Michael Poddlesak, WSD
Timothy Sills, WSD
Ninh Duong, WSD

Electronics and Surveillance Research Laboratory
Head Image Analysis and Exploitation Group, SSD
Head Surveillance Systems Assessment Group, SSD
Head Imaging EO Systems, SSD
Geoff Burls, SSD
Frank Lui, LOD

DSTO Library and Archives

Library Fishermans Bend (Doc Data Sheet)
Library Maribyrnong (Doc Data Sheet)
Library Salisbury
Australian Archives
Library, MOD, Pyrmont (Doc Data sheet only)
US Defense Technical Information Center, 2 copies
UK Defence Research Information Centre, 2 copies
Canada Defence Scientific Information Service, 1 copy
NZ Defence Information Centre, 1 copy
National Library of Australia, 1 copy

Capability Systems Staff

Director General Maritime Development (Doc Data Sheet only)
Director General Aerospace Development

Knowledge Staff

Director General Command, Control, Communications and Computers
(DGC4) (Doc Data Sheet only)
Director General Intelligence, Surveillance, Reconnaissance, and Electronic Warfare
(DGISREW)R1-3-A142 CANBERRA ACT 2600 (Doc Data Sheet only)
Director General Defence Knowledge Improvement Team (DGDKNIT)
R1-5-A165, CANBERRA ACT 2600 (Doc Data Sheet only)

Army

Stuart Schnaars, ABCA Standardisation Officer, Tobruk Barracks, Puckapunyal,
3662(4 copies)
SO (Science), Deployable Joint Force Headquarters (DJFHQ) (L), MILPO
Gallipoli Barracks, Enoggera QLD 4052 (Doc Data Sheet only)
NPOC QWG Engineer NBCD Combat Development Wing, Tobruk Barracks,
Puckapunyal, 3662 (Doc Data Sheet relating to NBCD matters only)

Intelligence Program

DGSTA Defence Intelligence Organisation
Manager, Information Centre, Defence Intelligence Organisation

Corporate Support Program

Library Manager, DLS-Canberra

UNIVERSITIES AND COLLEGES

Australian Defence Force Academy

Library

Head of Aerospace and Mechanical Engineering

Serials Section (M list), Deakin University Library, Geelong, 3217

Hargrave Library, Monash University (Doc Data Sheet only)

Librarian, Flinders University

OTHER ORGANISATIONS

NASA (Canberra)

AusInfo

OUTSIDE AUSTRALIA

ABSTRACTING AND INFORMATION ORGANISATIONS

Library, Chemical Abstracts Reference Service

Engineering Societies Library, US

Materials Information, Cambridge Scientific Abstracts, US

Documents Librarian, The Center for Research Libraries, US

INFORMATION EXCHANGE AGREEMENT PARTNERS

Acquisitions Unit, Science Reference and Information Service, UK

Library - Exchange Desk, National Institute of Standards and Technology, US

National Aerospace Laboratory, Japan

National Aerospace Laboratory, Netherlands

SPARES (5 copies)

Total number of copies: 60

| | | | | | |
|--|------------------------------|-----------------------------|---|---|----------------------------|
| DEFENCE SCIENCE AND TECHNOLOGY ORGANISATION DOCUMENT CONTROL DATA | | | | | |
| | | | | 1. PRIVACY MARKING/CAVEAT (OF DOCUMENT) | |
| 2. TITLE Validation of the SensorVision Thermal Emission Model | | | 3. SECURITY CLASSIFICATION (FOR UNCLASSIFIED REPORTS THAT ARE LIMITED RELEASE USE (L) NEXT TO DOCUMENT CLASSIFICATION) Document (U) Title (U) Abstract (U) | | |
| 4. AUTHOR(S) Ninh Duong and Michael Wegener | | | 5. CORPORATE AUTHOR Aeronautical and Maritime Research Laboratory 506 Lorimer St Fishermans Bend Victoria 3207 Australia | | |
| 6a. DSTO NUMBER DSTO-RR-0212 | | 6b. AR NUMBER AR-011-866 | | 6c. TYPE OF REPORT Research Report | |
| | | | | 7. DOCUMENT DATE April 2001 | |
| 8. FILE NUMBER J9505/21/6 | 9. TASK NUMBER Air 99/133 | 10. TASK SPONSOR DASD | 11. NO. OF PAGES 76 | | 12. NO. OF REFERENCES 6 |
| 13. URL on the World Wide http://www.dsto.defence.gov.au/corporate/reports/DSTO-RR-0212.pdf | | | 14. RELEASE AUTHORITY Chief, Weapons Systems Division | | |
| 15. SECONDARY RELEASE STATEMENT OF THIS DOCUMENT <i>Approved for public release</i> | | | | | |
| OVERSEAS ENQUIRIES OUTSIDE STATED LIMITATIONS SHOULD BE REFERRED THROUGH DOCUMENT EXCHANGE, PO BOX 1500, SALISBURY, SA 5108 | | | | | |
| 16. DELIBERATE ANNOUNCEMENT No Limitations | | | | | |
| 17. CASUAL ANNOUNCEMENT Yes | | | | | |
| 18. DEFTTEST DESCRIPTORS Hardware in the loop, Infrared images, Models, Environment simulation | | | | | |
| 19. ABSTRACT <p>The Systems Simulation Centre of the DSTO is currently considering the implementation of a commercial-off-the-shelf software package called SensorVision to fulfil the scene generation function of an infrared hardware-in-the-loop (HIL) system. Before the software can be used for the intended application, there is a need to verify and validate the SensorVision models to ensure that the generated scenes are sufficiently realistic for HIL simulation purposes. This report discloses the results and conclusions of a validation effort focused on the SensorVision thermal emission model, which includes both the surface temperature prediction of objects and the thermal radiance calculations. It is shown that the thermal emission model employed by SensorVision has errors that can affect the level of realism associated with the generated infrared images. Unrealistic scenes can cause spurious HIL simulation results, since these infrared images are used as the primary stimuli for the system being tested.</p> <p>A procedure for providing confidence in HIL simulation results is recommended, involving general guidelines for simulation construction and post-processing operations to provide users with image error indications.</p> | | | | | |

